이학박사 학위논문

Studies on the Heterogeneous Modifications and Applications of Palladium-Catalyzed Suzuki Coupling Reaction

팔라듐 촉매를 이용한 스즈키 반응의 비균질성 촉매반응 및 그 응용에 관한 연구

2020년 2월

서울대학교대학원
화학부유기화학전공

권태희

이학박사 학위논문

Studies on the Heterogeneous Modifications and Applications of Palladium-Catalyzed Suzuki Coupling Reaction

지도교수 김 병 문

이 논문을 이학박사 학위논문으로 제출함

2020년 2월

서울대학교대학원
화학부 유기화학전공

권 태 희

권태희의 이학박사 학위논문을 인준함
2020년 2월

Chair _____(Seal)
Vice Chair _____(Seal)
Examiner _____(Seal)
Examiner _____(Seal)
Examiner _____(Seal)

Abstract

Described in this thesis are the heterogeneous modifications and various applications of the palladium-catalyzed Suzuki coupling reaction. Homogeneous palladium catalysts have been successfully employed for the Suzuki coupling reaction, however, they possess some drawbacks such as metal contamination into products, difficulty in recovery of the catalyst after reactions, high cost of the catalyst and so forth. To overcome the drawbacks of homogeneous Pd catalytic systems, the heterogeneous catalytic systems are studied in **Chapter 2**. Palladium nanoparticles on ionic polymer-doped graphene (**Pd-IPG**) nanocomposite catalysts have been investigated for efficient heterogeneous Suzuki coupling reactions. This combination effected highly accelerated Suzuki coupling reactions due to several advantageous features associated with the flanking ionic polymer part of the catalyst system. These include a high level of Pd incorporation, excellent dispersion stability, and increased accessibility and diffusion of the substrates onto the surface of Pd NPs.

A study on the application of the Suzuki-coupling reactions, which are applied in the field of organic light emitting diodes (OLED) material synthesis, is described in **Chapter 3**. We report the design, synthesis, and evaluation of new thermally activated delayed fluorescence (TADF) molecules possessing a sterically twisted skeleton by interlocking donor and acceptor moieties through a C-C bond. Strategic use of well-planned Pd-catalyzed Suzuki coupling reaction between two carefully designed partners was critical in the successful construction of the new TADF emitters. Compared to C-N-bond TADF molecules, such as **CPT2**, the newly introduced C-C bond TADF molecules show a singlet–triplet energy-gap decrease to less than 0.22 eV because of the

steric hindrance caused by the direct C-C bond connection. With the introduction of dibenzofuran core structure, devices comprising **BMK-T317** and **BMK-T318** exhibit magnificent display performance, especially their external quantum efficiencies, which is as high as 19.9 and 18.8%, respectively. Moreover, the efficiency roll-off of **BMK-T318** improves significantly (26.7%). These results indicate that the material stability can be expected through the reduction of their singlet-triplet splitting and the precise adjustment of dihedral angles between the donor–acceptor skeletons.

Keyword: Suzuki coupling reaction; Cross-coupling reaction; Heterogeneous catalysis; Palladium nanoparticle; Ionic polymer-doped graphene; OLED materials, Thermally activated delayed fluorescence (TADF), blue TADF emitters.

Student Number: 2013-30087

Table of Contents

List of Figures

(the reaction was catalyzed by Pd-IPG and performed under the optimized conditions).

Figure III-1. Chemical structures and dihedral angle, natural transition orbital (NTO) hole (blue) and acceptor (red), and HOMO and LUMO orbital distributions.

Figure III-2. Optical absorption and photoluminescence spectra of (a) **BMK-T138**, (b) **BMK-T139**, (C) **BMK-T317**, and (d) **BMK-T318**.

Figure III-3. Overlap density-delayed fluorescence lifetimes (τ_{DF}) data

Figure III-4. hole current versus HOMO energy

Figure III-5. **BMK-T138, BMK-T139, BMK-T317, and BMK-T318** TADF devices with an mCBP-CN (15%) host: (a) current (J–V–L); (b) external quantum efficiency and current efficiency versus current density curves.

Figure III-6. The EL spectra of **BMK-T138**, **BMK-T139**, **BMK-T317**, and **BMK-T318** TADF devices.

List of Schemes

15a = 48%, **15b** = 42%; c) $Pd(Ph_3)_4$, 1 M K_2CO_3 in H_2O, THF, 80 ^oC, **BMK-T236** = 45%, **BMK-T237** = 69%.

Scheme III-4. Synthetic routes of **BMK-T317**. a) Carbazole, NaH, DMA, 160 ^oC, 44%; b) trimethyl borate, n-BuLi, THF, -78 ^oC, then 2 N HCl, r.t., 51%; c) $Pd(Ph_3)_4$, 1 M K_2CO_3 in H_2O, THF, 80 ^oC, 45%.

Scheme III-5. Synthetic routes of **BMK-T318**: a) Carbazole, NaH, DMA, 160 ^oC, 19%; b) trimethyl borate, n-BuLi, THF, -78 ^oC , then 2 N HCl, r.t., 55%; c) $Pd(PPh_3)_4$, 1 M K_2CO_3 in H_2O, THF, 80 ^oC, 45%.

List of Tables

Chapter 1. Introduction

In synthetic organic chemistry, the development of efficient synthetic methods for the construction of carbon-carbon (C-C) bonds have been of paramount importance. Traditionally many synthetic methods have been developed for the C-C bond forming reactions including anionic aldol type, cationic Friedel-Crafts type, radical-mediated, and pericyclic reactions.[1-11] Meanwhile, novel transition metal-catalyzed methodology has recently attracted enormous interest.[12-17] Especially, Pd-catalyzed Suzuki-coupling transformations constitute a powerful methodology for the formation of various kinds of C-C bonds.[18-20] The reaction features several beneficial points such as high convergence in synthetic strategy, tolerance to a broad range of functional groups, insensitivity towards water, and generally high regio- and stereo-selectivities.[21-23]

To date, the Suzuki-coupling reactions have been conventionally performed primarily through the use of homogeneous Pd catalysts.[24,25] However, Pd-catalyzed homogeneous reactions have suffered from limitations such as the requirement of toxic and air-sensitive phosphine ligands, safety issues of products due to metal contamination and difficulties in catalyst recovery and recycling.[26,27] Tireless efforts toward alleviating these shortcomings have continued and development of heterogeneous catalytic systems employing various supports to Pd nanoparticles (NPs) came as one remedy favorably leading to effective retaining of catalytic activity and promoting durability of the catalyst because of maximized active surface area and enhanced anchoring ability.[28-31] A new type of support for heterogeneous catalysts is described in the **Chapter 2**.

Transition-metal catalyzed cross coupling reactions have emerged as an efficient method for the installation of C–C bonds for compounds employed in new material development in recent decades. The ability

to activate a wide range of bonds, milder reaction conditions, and excellent functional group tolerance are some of the major features that have made transition-metal catalyzed reactions an essential tool in organic synthesis.[32-36] As their applications range from synthesizing simple biaryls to complex natural products and functional molecules, especially, Pd-catalyzed cross coupling reactions are also useful in the field of electronic materials such as organic light emitting diodes (OLED).[37-42]

The emission of electromagnetic radiation from organic material, such as anthracene, has been first discovered in 1963. A. J. Heeger, A. G. MacDiarmid, and H. Shirakawa were awarded the 2000 Nobel Prize in Chemistry from their studies on the possibility to obtain conductive organic thin films using π-conjugated materials (poly-acetylene).

After their first development of conductive polymer in the late 1980s, OLEDs slowly made their entry into the market of displays for televisions and mobile phones. Compared to other display technologies, OLED displays offer advantages such as wide viewing angles and very high contrast ratio while maintaining low energy consumption. In addition, OLED displays are thin and lightweight and can even be fabricated on flexible substrates, which allows for new and exciting applications. Therefore, OLEDs have been considered powerful components of lighting devices. They have enormous potential application to general lighting, larger displays, and flexible displays.[43-48] However, the first-generation OLEDs (fluorescent emitters) demonstrated in 1987 have limitations such as low efficiency, because only 25% of the singlet excitons can be harvested in accordance with quantum mechanics. It can be greatly improved to 100% with the incorporation of heavy-metal atoms into the organic molecules, which facilitates phosphorescent emission, which is called a second

generation emitter as shown in the **Figure I-1**. However, the operation lifetime is still a bottleneck for blue phosphorescent-OLEDs. Due to their wide bandgap (~ 3 eV) and long exciton lifetime (~ μs), exciton and polaron interactions create a hot excited state (~ 6 eV), which degrades the material.[49-51] Tireless efforts toward increasing the efficiency and stability of OLEDs have continued, and various photophysical phenomena in the fields of OLEDs have been discovered, such as singlet fission, triplet–triplet annihilation, and thermally activated delayed fluorescence (TADF).[49]

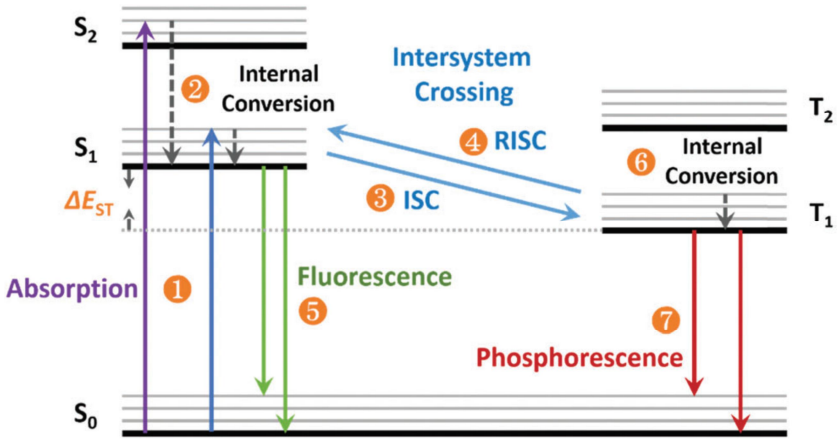

Figure I-1. The transition process of photogenerated excitons for fluorescence, phosphorescence, and TADF in organic molecules.[51]

A TADF emitter reduces the energy difference (ΔE_{ST}) between the singlet and triplet states through molecular design, so that triplet excitons may upconvert into the singlet state by thermal energy through reverse intersystem crossing (RISC). A 100% internal quantum efficiency (IQE) can be achieved by using a TADF emitter, which avoids the use of heavy atoms inside the organic material. This is called a third generation emitter. However, this still does not solve the

problem of the short lifetime for deep blue-OLEDs, which is also caused by the high triplet energy and long triplet lifetime. The short material lifetime of TADF technology is a major obstacle to the development of economically feasible, highly efficient, and durable devices for commercial applications. TADF devices are also hampered by insufficient operational stability. Because the average bond energy of a C-C bond is stronger than that of a C-N bond, new TADF emitters having interlocked acceptor units on their backbone structure are desirable, which can be obtained via C-C bond connections.

An application of the C-C bonds formations for TADF materials is described in **Chapter 3.**

Chapter 2.

Recyclable Pd-Graphene Hybrid Catalysts Tuned by Ionic Polymers: Efficient Suzuki Coupling Reactions

*Part of this thesis was published in *RSC Advances,* **2017**, *7*, 11684.

2.1. Introduction

For desirable catalytic performance of heterogeneous Pd catalysts, various carbon supports of Pd NPs have been developed, such as functionalized carbon nanotubes (CNTs), graphenes and their combinations.[52-60] These approaches have been somewhat successful in solving the issues associated with the homogenous catalysis system, however, the limited functional groups on the carbon supports often caused detrimental aggregation through long range π-π stacking and weak interfacial interaction with Pd NPs, leading to low quality incorporation, easy dissolution and loss of Pd NPs from the support, and ambiguous dispersion stability.[61-63]

Recently efforts to overcome these limitations have emerged through employment of non-covalently functionalized carbon supports equipped with polymer compatibilizers.[64-66] These systems allowed for a great nanocomposite catalyst with uniform and well-distributed Pd NPs on the carbon supports as well as noticeably enhanced catalytic performance due to better dispersion property, strong interfacial linking, and adequate interaction with substrates.[30,67-70] Specifically, in our recent report, the ionic polymer-doped graphene support was explored to develop effective catalysts for hydrogenation reaction through combination with fine-sized Pd NPs (1-3 nm), resulting in the ultra-accelerated catalytic reduction of methylene blue. Effective interaction and diffusion of reacting species onto the surface of Pd NPs along with its desirable dispersion property in the aqueous medium were believed to be the main reason for the successful catalytic activity.[69] However, the fine-sized metal NPs can be generally less stable under harsh reaction conditions, such as high temperature and the presence of a strong base.[71]

Herein, we demonstrate that the combination of multi-scaled Pd NPs with ionic polymer-doped reduced graphene oxide (rGO) supports (Pd-IPG) culminated in markedly enhanced catalytic activity (TOF: 990 h-1) and yield (> 99%) in the Suzuki coupling reaction between iodobenzene and phenylboronic acid in comparison to that of the catalyst without the ionic polymer (Pd-rGO). The Pd-IPG nanocomposite catalysts showed good recyclability during 10-time repeated cycles.

2.2. Results and Discussion

The multi-scaled Pd NPs loaded on the pyrene functionalized poly(dimethylaminoethyl methacrylate)-b-poly[(ethylene glycol) methyl ether methacrylate] ionic polymer-doped graphene support (Pd-IPG) were synthesized by a facile in-situ method (**Scheme II-1** and **II-2**), which used sodium tetrachloropalladate as a metal precursor, benzoic acid (BA) as a structure-directing agent, N,N-dimethyl formamide (DMF) as a solvent and a reducing agent.

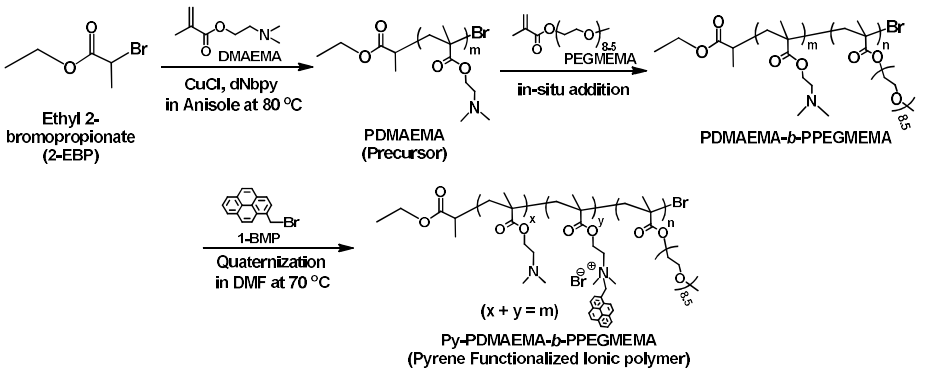

Scheme II-1. Synthesis of pyrene functionalized PDMAEMA-*b*-PPEGMEMA ionic polymer.

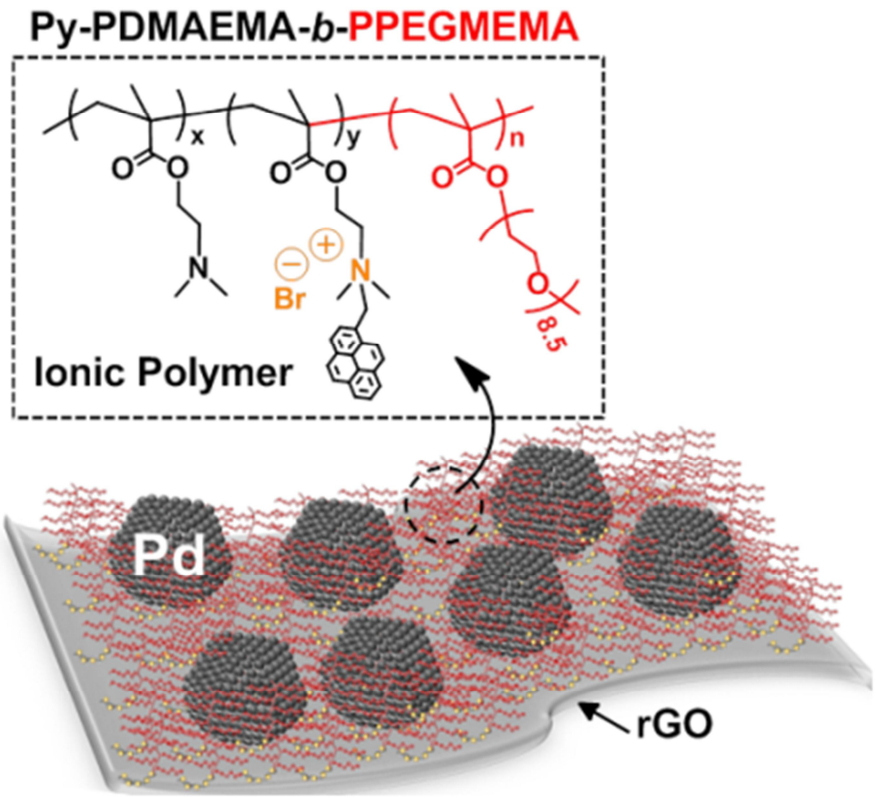

Scheme II-2. Illustration of the Pd-IPG nanocomposite catalyst with the chemical structure of pyrene functionalized poly(dimethylaminoethyl methacrylate)-b-poly[(ethylene glycol) methyl ether methacrylate] (Py-PDMAEMA-b-PPEGMEMA) ionic polymer on the rGO support.

The acquired Pd-IPG nanocomposite catalysts were characterized through scanning transmission electron microscopy (STEM), which exhibited well-distributed multi-scaled Pd NPs on the IPG (**Figure II-1A**). STEM energy-dispersive X-ray (STEM-EDX), powder X-ray diffraction (XRD), and X-ray photoelectron spectroscopy (XPS) analyses of Pd-IPG were performed for the investigation of the composition and structure of Pd NPs on IPG. The STEM-EDX elemental mapping of Pd-IPG showed that the observed NPs comprised Pd atoms, and the STEM-EDX spectrum exhibited 49.7 wt% of Pd

relative to C, O, and N contents originated from IPG (Figure I-1B and 1C, respectively).

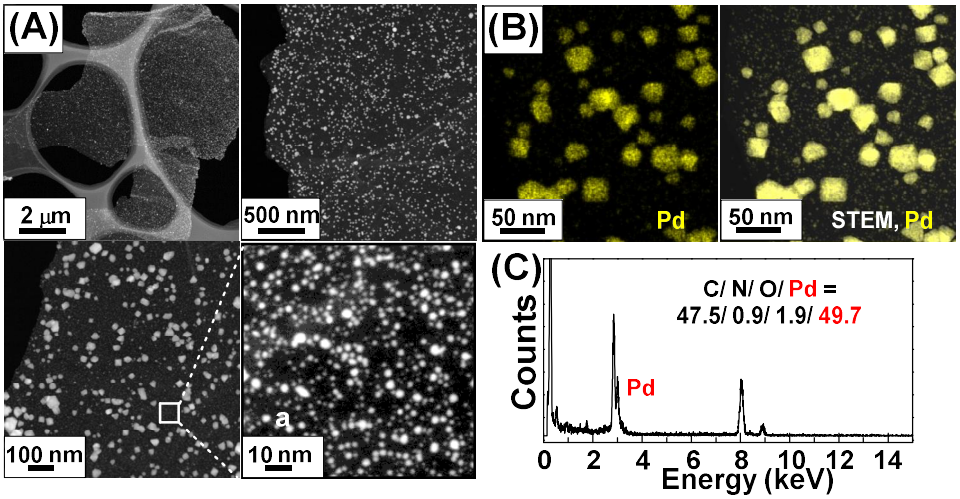

Figure II-1. (A) STEM images (inset a: magnified image for small-sized Pd NPs, size distribution 3-5 nm), (B) STEM-EDX elemental mapping images for Pd, and (C) STEM-EDX spectrum of Pd-IPG.

For comparison, Pd NPs loaded rGO without the ionic polymer (Pd-rGO, Pd: 42.7 wt%) was synthesized using the same conditions for the synthesis of the Pd-IPG and characterized as shown in the **Figure II-2**. The STEM images of Pd-rGO showed relatively aggregated and partially decorated Pd NPs on the rGO support (**Figure II-2A**). The content of Pd NPs in Pd-rGO (42.7 wt.%) was almost similar to that of Pd-IPG (49.7 wt.%).

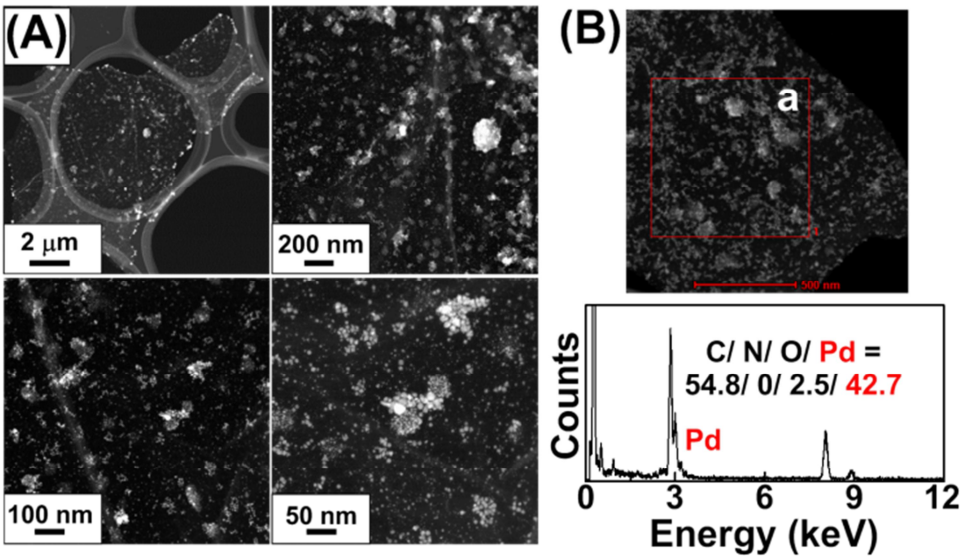

Figure II-2. (A) Representative STEM images and (B) STEM-EDX spectrum of Pd-rGO scanned on the region marked on inset a.

The XRD patterns of Pd-IPG showed predominant peaks at 25.1°, 39.5 °, 45.9 °, 67.0° corresponding to the face-centered cubic (FCC) structure, except for the broad peak at 25.1°, which can be originated from the IPG carbon support (**Figure II-3A**).[30,72] Moreover, the average crystalline size of Pd NPs on IPG was evaluated to be 8.4 nm from the XRD pattern with the relation of Scherrer formula, which was in good agreement with corresponding STEM analysis exhibiting the broad distribution of Pd NPs in a size (large numbers: 2-5 nm, small numbers: 15-30 nm), as described in **equation II-1** and **Table II-1**.[10] The average crystalline size of Pd NPs in Pd-IPG was calculated by the relation of Scherrer equation:

$$D_S = \frac{K\lambda}{\beta_{hkl}cos\theta} \qquad \textbf{(Equation II-1)}$$

where D is crystalline size, K is shape factor (0.9), λ is wavelength of

Cukα radiation, and β_{hkl} is full width of half maximum (FWHM).

Table II-1. Structural parameters of Pd-IPG.

Catalyst	2θ	*d* (nm)	β_{hkl}	FWHM (rad)	D_S[a] (nm)	D_{STEM}[b] (nm)
Pd-IPG	39.5	0.22	(111)	0.02670	8.4	Large numbers (3-5 nm), Small numbers (15-30 nm)

[a] D_S was deduced from the relation of Scherrer formula. [b] D_{STEM} was measured by using STEM images.

The deconvoluted XPS Pd 3d spectra of Pd-IPG showed predominant peaks at 334.7/340.0 eV and 336.0/340.9 eV corresponding to Pd^0 and Pd^{2+}, respectively (**Figure II-3B**).[56] The XPS result indicated that the Pd NPs in Pd-IPG mainly comprises the metallic state Pd.

The interfacial interaction of three components including rGO, ionic polymer, and Pd NPs in Pd-IPG was characterized through Raman spectroscopy (**Figure II-3C**). Due to the presence of the ionic polymer to rGO, the predominant peaks of the rGO Raman spectrum at 1339.1 and 1582.5 cm^{-1} corresponding to D and G bands were shifted to higher wavenumbers to 1347.1 and 1585.4 cm^{-1}, respectively. After incorporation of IPG with Pd NPs, these two bands were also slightly shifted to 1348.2 and 1589.6 cm^{-1}. These positive Raman shifts can be explained by the influence of intermolecular electron-transfer, indicating the well-developed intercalation structure.[69]

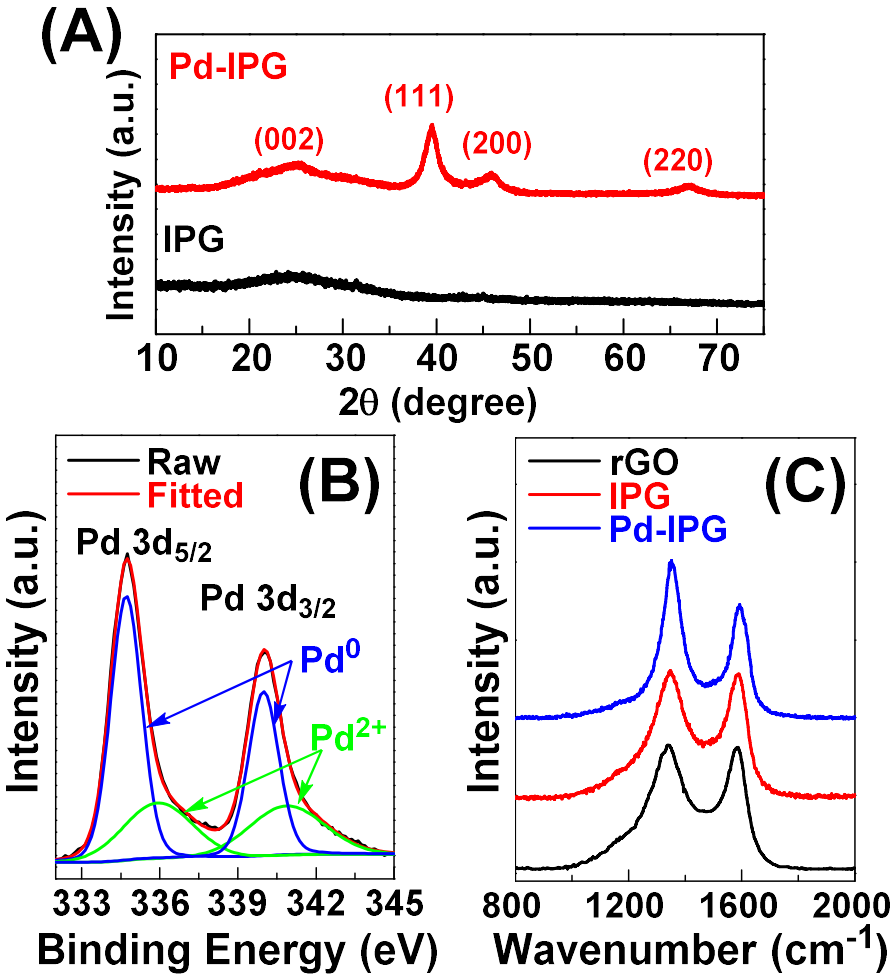

Figure II-3. (A) Powder XRD patterns of IPG and Pd-IPG. (B) XPS Pd 3d spectrum of Pd-IPG. (C) Raman spectra of rGO, IPG, and Pd-IPG.

To optimize the catalytic reaction conditions of Pd-IPG, Suzuki coupling reactions using iodobenzene and phenylboronic acid as model substrates were screened with regard to various bases and solvents (**Table II-2**). The reactions were first screened with various bases at 60 ^{o}C with 0.3 mol% Pd-IPG in ethanol/water (v/v = 1:1) (**Table II-2**, entries 1-6). As shown, reactions using most inorganic bases proceeded furnishing high yields (> 98%) except for that with $KHCO_3$ (81%), indicating that strong bases are more effective than weak ones. Whereas,

TEA, an organic base, was much less effective in this system. To identify the best base for this system, the content of Pd-IPG was reduced from 0.3 mol% to 0.1 mol%, and NaOH still showed sustained reactivity with high yield (99%). However, Na_2CO_3 showed noticeably reduced yield from 99% to 60% after the catalyst content was decreased to 0.1 mol%. From the base screening tests, the most optimal Suzuki coupling reaction with Pd-IPG was achieved through the use of NaOH.

Table II-2. Optimization of the reaction conditions for Suzuki coupling reactions between iodobenzene and phenylboronic acid catalyzed by the Pd-IPG nanocomposite catalysts.[a]

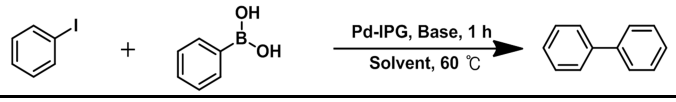

Entry	Solvent	Base	Cat. (mol%)	Yield[b] (%)
1	EtOH:H_2O=1:1	TEA	0.3	51
2	EtOH:H_2O=1:1	$KHCO_3$	0.3	81
3	EtOH:H_2O=1:1	K_2CO_3	0.3	98
4	EtOH:H_2O=1:1	Cs_2CO_3	0.3	98
5	EtOH:H_2O=1:1	Na_2CO_3	0.3	99
6	EtOH:H_2O=1:1	NaOH	0.3	>99
7	EtOH:H_2O=1:1	NaOH	0.2	99
8	EtOH:H_2O=1:1	NaOH	0.1	99
9	EtOH:H_2O=1:1	Na_2CO_3	0.1	60
10	H_2O	NaOH	0.1	20
11	MeOH	NaOH	0.1	83
12	EtOH	NaOH	0.1	86
13	CH_3CN	NaOH	0.1	1
14	DMF	NaOH	0.1	NR
15	THF	NaOH	0.1	NR
16	DMF:H_2O=1:1	NaOH	0.1	50
17	THF:H_2O=1:1	NaOH	0.1	48

[a] Reaction conditions: Iodobenzene (0.1 mmol), Phenylboronic acid (0.12 mmol), base (0.2 mmol), and solvent (0.8 mL) at 60 ^{o}C under air. [b] Yields were calculated from GC analysis with anisole as an internal standard.

With the NaOH in hand as an optimal base for this system, representative protic (H_2O, MeOH, EtOH) and aprotic solvents (CH_3CN, THF) were screened for the reaction with Pd-IPG. Reactions in protic solvents, except for water, proved to proceed with much better reactivity in comparison to those in aprotic ones (**Table II-2**, entries 11-12 vs. 13-15, respectively). This result could be attributed to the poor solubility of NaOH in aprotic solvents. To confirm the solubility issue of NaOH in aprotic solvents, aqueous solutions of either THF or DMF were applied for the Suzuki coupling reaction and the results clearly supported the proposed reason for low reactivity in the cases of the aprotic solvents (**Table II-2**, entries 16-17). Meanwhile, the use of water only as a solvent produced only 20% yield despite good solubility of NaOH, presumably due to the poor solubility of the organic substrates in water. As such, the Suzuki coupling reaction at 60 ^{o}C using NaOH as a base in EtOH/H_2O (v/v = 1:1) as a solvent was selected as an optimized condition for the reaction employing 0.1 mol% of Pd-IPG.

The optimized reaction protocol for the Suzuki coupling reaction between various substituted aryl halides and aryl boronic acids was applied to evaluate the catalytic activity of Pd-IPG using Pd-rGO as a reference catalyst, and corresponding yields and turnover frequency (TOF) values were summarized in **Table II-3**. The use of Pd-IPG (0.1 mol%) in the coupling reaction between iodobenzene and phenylboronic acid showed high catalytic activity, with 99% yield in 1 h and the TOF value of 990 h^{-1}, and the reactivity employing the Pd-IPG catalyst was largely dictated by the electronic nature of

substituents in aryl iodides; aryl iodides with an electron withdrawing substituent showed higher catalytic activity relative to those with electron-donating substituents. Specifically, the reaction with aryl iodide having an acetyl substituent showed 2-fold higher TOF value (2000 h^{-1}) for the coupling product than that of iodobenzene, and achieved 8-fold higher TOF value in comparison to the corresponding hydroxyl-substituted aryl iodide (245 h^{-1}, **Table II-3**, entries 1, 2 and 4, respectively).

Table II-3. Evaluation of catalytic activity of Pd-IPG and Pd-rGO according to the various substrates under optimized conditions.[a]

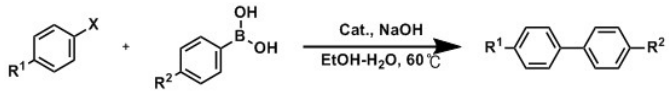

Entry	Catalyst	X	R^1	R^2	Time	Yield[b]	TOF[c] (h^{-1})
1	Pd-IPG[d]	I	H	H	1 h	99%	990
2		I	4-COMe	H	0.5 h	100%	2000
3		I	4-OMe	H	3 h	91%	303.3
4		I	4-OH	H	4 h	98%	245
5		I	H	4-OMe	1 h	97%	970
6		I	H	4-OH	24 h	42%	17.5
7		Br	H	H	24 h	24%	10.0
8		Br	4-COMe	H	24 h	100%	41.7
9	Pd-rGO[e]	I	H	H	3 h	92%	61.3
10		I	4-COMe	H	2 h	95%	95
11		I	4-OMe	H	6 h	91%	30.3
12		I	4-OH	H	3 h	93%	62
13		I	H	4-OMe	2 h	100%	100
14		I	H	4-OH	24 h	76%	6.3
15		Br	H	H	24 h	5%	0.4
16		Br	4-COMe	H	24 h	56%	4.7

[a] Reaction conditions: Aryl halide (0.1 mmol), Arylboronic acid (0.12 mmol), NaOH (0.2 mmol, and EtOH/H_2O (0.8 mL) at 60 ^oC under air. [b] GC yield were calculated by using anisole as an internal standard. [c] TOF value was calculated by moles of product with per mole of Pd catalyst per hour. [d] Pd-IPG (0.1 mol% to aryl halide). [e] Pd-rGO (0.5 mol% to aryl halide).

It is intriguing to note that for the production of 4-methoxy-1,1'-biphenyl the reaction between 4-methoxyphenylboronic acid and phenyl iodide (entry 5) is a much better choice with 3-fold higher TOF value (970 h^{-1}) compared to that of 4-methoxyphenyl iodide and phenylboronic acid (entry 3). However, the reaction of 4-hydroxyphenylboronic acid led to a considerable decrease in the reactivity with iodobenzene (**Table II-3**, entry 6). These results indicate that the rates of coupling reactions using Pd-IPG are quite sensitive to the electronic nature of the substrates and the selection of appropriate substrates is necessary for more effective coupling reactions.

To explore the ionic polymer doping effect, the Suzuki coupling reactions with the same substrates employing Pd-rGO as a reference catalyst were examined (**Table II-3**, entries 9-16). Since the reactions employing 0.1 mol% Pd-rGO required significantly long reaction time (over 24 h), 0.5 mol% Pd-rGO was employed for the comparison reaction. The activity profile of Pd-rGO with respect to the electronic nature of the substrates including aryl bromides was fully identical to that of the corresponding Pd-IPG. However, the catalytic activities of Pd-rGO were significantly lower for all substrates than that of Pd-IPG, exhibiting 21-fold maximum TOF reduction in the case of entry 10 compared to entry 2 (**Table II-3**).

The Suzuki coupling reactions with bromide substrates were performed to evaluate the comparative reactivity of the Pd-IPG to the Pd-rGO as a reference catalyst (**Table II-3**, entries 7,8,15, and 16). The improved reactivity of Pd-IPG based on the ionic polymer doping effect was also prominent in the case of reactions with bromide substrates, specifically furnishing almost 9-fold maximum enhancement in the reaction of acetyl-substituted aryl bromide with phenylboronic acid

(**Table II-3**, entries 8 and 16). However, the TOF values in the reaction with bromide substrates suggest that the absolute reactivity was relatively degraded in comparison to the reaction with iodide substrates (**Table II-3**).

The highly enhanced catalytic activities of Pd-IPG relative to Pd-rGO can be explained by two possible reasons: (i) the doped ionic polymers on rGO render the system to exhibit good affinity in the aqueous medium, leading to the better dispersion of the Pd-IPG in the reaction medium. As such, the accessibility of substrates and the availability of the catalyst can be substantially enhanced in comparison to those of Pd-rGO. (ii) Upon the basis of the reaction mechanism, the strong cohesion of arylboronic acid and possibly some soluble Pd species detached from the NPs with the long ethylene oxide groups in the ionic polymers can facilitate the effective diffusion of reacting species together in the vicinity of the Pd NPs, leading to the accelerated coupling reaction (**Figure II-4**). However, the reason for low catalytic activity in the Suzuki coupling reactions with bromide substrates should be addressed and we found that the catalytic activity is considerably governed by an active surface area, which is mainly related to the metal NP size. The report by Mülhaupt et al. provides important information to address the effects of the NP size on the reactivity.[52] Based on the Mülhaupt's study, we realized that the size effect of Pd NPs is more important than the effect of functionalized supports for enhanced catalytic activity. Furthermore, Mülhaupt's report also expressed that the lager content of oxygenated carbons in the graphene support can promote Suzuki-coupling reactions and this effect corroborated the advantages of the ionic polymer doping in the Pd-rGO catalysts.

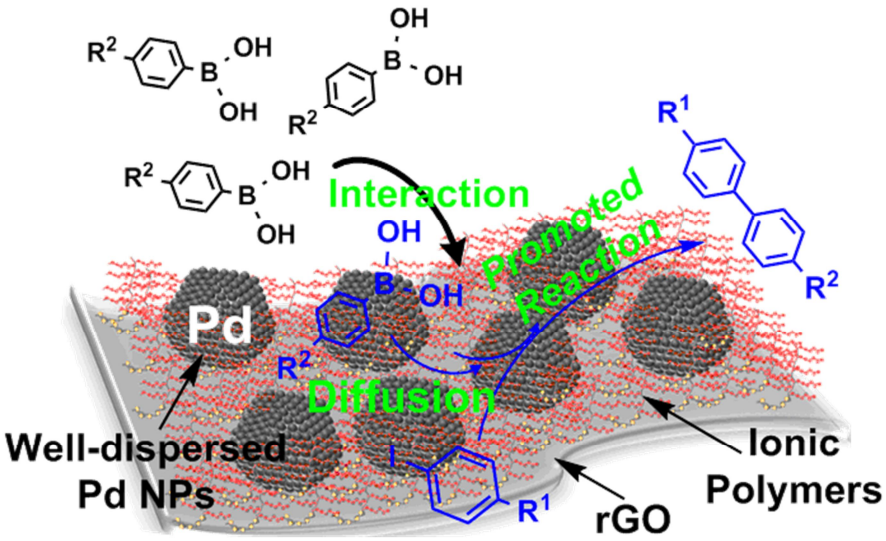

Figure II-4. Schematic illustration of the Pd-IPG nanocomposite catalyst's role on the reaction between aryl iodides and arylboronic acids.

Comparative evaluation of the Pd-IPG catalyst was performed in contrast with previously reported, state-of-the-art heterogeneous catalysts for the Suzuki coupling reaction. **Table II-4** lists the results of the coupling reactions between iodobenzene and phenylboronic acid employing various heterogeneous catalyst systems. Reactions with most of the listed catalysts proceeded with high yields (> 90%). However, in many cases rather harsh reaction conditions were used in comparison to that of Pd-IPG, for example use of toxic solvents (DMF or DME), higher temperature, and longer reaction time. The Pd-IPG exhibited higher catalytic activity (TOF: 990 h^{-1}), than the carbon supported Pd catalysts including Pd/SiC-CNT, Pd/CNT-graphene hydrogel, and Pd-Fe_3O_4@C, which exhibited 350, 799, and 324 h^{-1} TOF values, respectively (**Table II-4**, entries 2, 4, and 8).[53,73,74] These results indicate that the Pd-IPG is an effective catalyst with high catalytic activity requiring environmentally clean reaction conditions for Suzuki coupling reactions.

Table II-4. Catalytic performances and reaction conditions of various Pd-based heterogeneous catalysts in the Suzuki coupling reaction of iodobenzene with phenylboronic acid.

Entry	Catalyst	Solvent	Base	Temperature (^{o}C)	Time (h)	Yield[a] (%)	TOF[b] (h^{-1})	Ref.
1	Pd-Fe_3O_4	DME-H_2O (3:1)	Na_2CO_3	Reflux	24.0	99	41	31
2	Pd/CNT-graphene	EtOH-H_2O (1:1)	K_2CO_3	60	0.25	>99	799	53
3	Silica@Pd-ZnMOF	EtOH	K_2CO_3	80	2.0	92	79	56
4	Pd-Fe_3O_4@C	EtOH	K_2CO_3	Reflux	1.0	100	325	73
5	Pd NPs	H_2O	Na_2CO_3	80	24.0	97	40	75
6	Pd/Polymer colloids	DMF-H_2O (1:1)	K_2CO_3	50	1.5	97	645	76
7	Pd-CNT	DMF	Na_2CO_3	110	24.0	94	13	77
8	Pd/SiC-CNT	EtOH-H_2O (4:1)	K_3PO_4	60	1.0	98	350	78
9	Pd-rGO	EtOH-H_2O (1:1)	NaOH	60	3.0	92	61	This Work
10	Pd-IPG	EtOH-H_2O (1:1)	NaOH	60	1.0	99	990	This Work

[a] GC yield was calculated by using anisole as an internal standard. [b] TOF value was calculated using the equation as follows TOF = $M_{sub} \times \text{Yield}(\%) \ / \ M_{cat} \times \text{Yield}(\%)$.

The Pd-IPG catalyst system was then evaluated for repeated use since recyclability of the catalysts is one of the most important issues in viewpoint of cost, and recycling of the Pd-IPG was investigated for ten repetitions of Suzuki coupling reactions with iodobenzene and phenylboronic acid as model substrates under the optimized conditions. As shown in **Table II-5** all reactions showed consistently high yields (> 96%).

After ten reaction cycles, the recovered Pd-IPG catalyst was characterized by STEM and STEM-EDX, which exhibited same morphology and a high level of retention in the Pd composition (Pd: 47.4 wt%) (**Figure II-5A** and **B**).

Table II-5. Recyclability tests of Pd-IPG for the Suzuki coupling reaction of iodobenzene with phenylboronic acid under optimized conditions.[a]

Runs	1st	2nd	3th	4th	5th	6th	7th	8th	9th	10th
Yield (%)	99	96	98	97	97	97	98	97	99	98

[a] Reaction conditions : Pd-IPG (0.1 mol%), Iodobenzene (0.1 mmol), Phenylboronic acid (0.12 mmol), base (0.2 mmol), and solvent (0.8 mL) at 60 ^{o}C under air for 1 h.

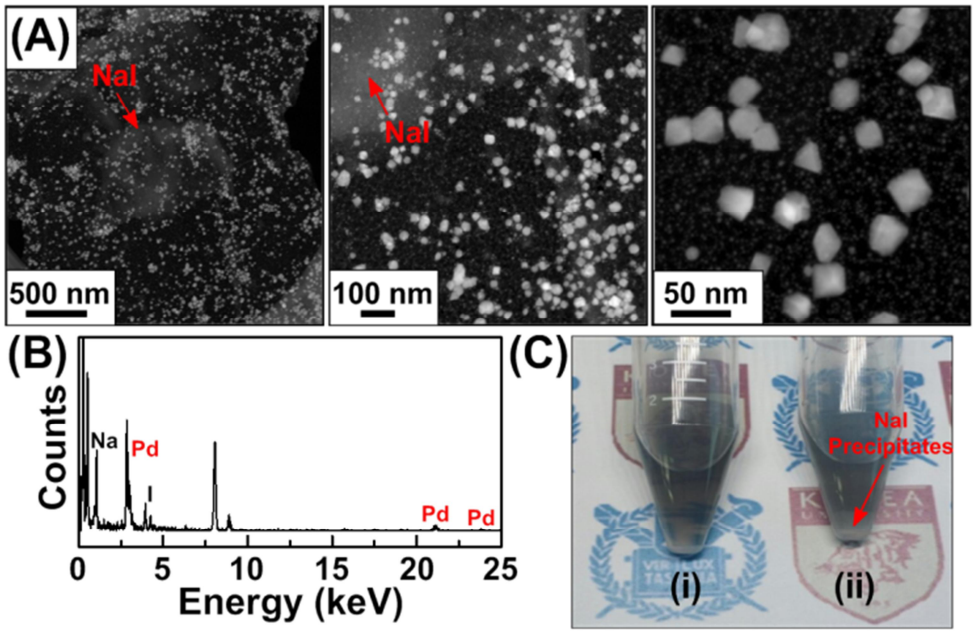

Figure II-5. (A) Representative STEM images and (B) STEM-EDX spectrum of Pd-IPG after ten repeated reaction cycles. (C) Photograph of the reaction solutions with Pd-IPG (i) before and (ii) after the recycle test (ten cycles).

For its reliability, further recyclability tests up to 20 cycles were performed. The large retention in the reactivity was observed up to the 14th cycle. However, the reactivity of the Pd-IPG started to decline at the 15th cycle (89% yield) and did not recover back to high yield (>95%) up to the 17th cycle (**Table II-6**). When we increased the reaction time from 1 h to 1.5 h, the reaction yield went up to >95%, as shown in **Table II-6**. The reason why it went up to 99% is not clear at this point, but the yields at the 18th to 20th recycling were equally high. The fact that there is an 'induction period' at the beginning of each reaction should also be considered.

Table II-6. Further recyclability tests of Pd-IPG for the Suzuki coupling reaction of iodobenzene with phenylboronic acid under optimized conditions.[a]

Runs	11th	12th	13th	14th	15th	16th	17th	18th	19th	20th
Yield (%)	99	96	98	95	89	91	87	97	99	98
Time (h)	1	1	1	1	1	1	1	1.5	1.5	1.5

[a] Reaction conditions : Pd-IPG (0.1 mol%), Iodobenzene (0.1 mmol), Phenylboronic acid (0.12 mmol), base (0.2 mmol), and solvent (0.8 mL) at 60 ^{o}C under air for 1 h.

On the basis of STEM studies, the primary reason for the degradation of the catalytic activity was the detrimental change of the Pd-IPG morphology (**Figure II-6**). These results indicate that the Pd-IPG's performance is dependable up to the 14th cycle, presumably owing to the strong interfacial linking ability of the ionic polymers. Furthermore, it should be mentioned that we observed insoluble white salts in the reaction mixture and the content gradually increased with increased repetition (**Figure II-5C (ii)**). This precipitate was analyzed to be sodium iodide (NaI) through STEM-EDX (**Figure II-5**). The NaI by-product was readily removed through filtration after dilution with water and the isolated Pd-IPG powder was redispersed in EtOH/ H_2O (v/v = 1:1) for further use.

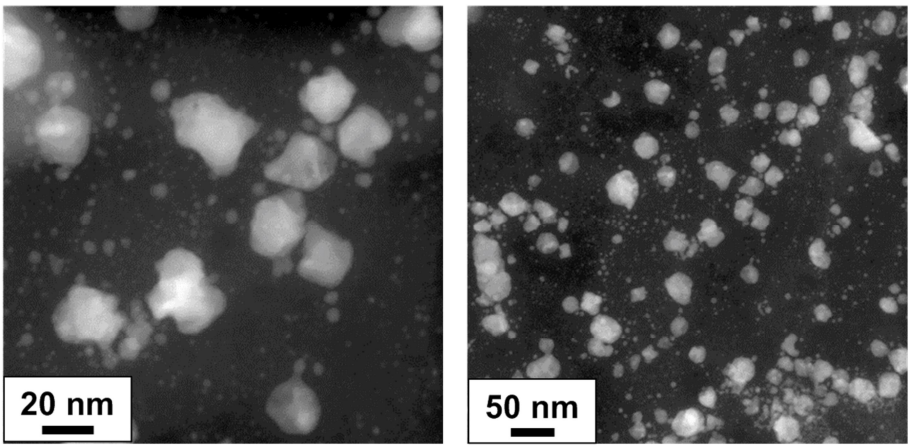

Figure II-6. Representative STEM images of the Pd-IPG after 20 repeated reaction cycles.

To explore the Suzuki coupling reaction mechanism employing the Pd-IPG catalyst, a hot-filtration test was performed from the reaction of iodobenzene with phenylboronic acid under the optimized conditions (**Figure II-7**).[56,74] The reaction mixture was examined the yields of the product biphenyl according to the Suzuki reaction every 15 minutes. After 30 min, when the reaction proceeded to give 35% yield, the reaction mixture was filtered to a preheated vial. The reaction from the filtrate after hot-filtration exhibited no increase in conversion up to 12 h, while the reaction with Pd-IPG continued to achieve 94% yield after 75 min. This result indicated that the Pd NPs on IPG hardly leached out during the Suzuki coupling reaction.

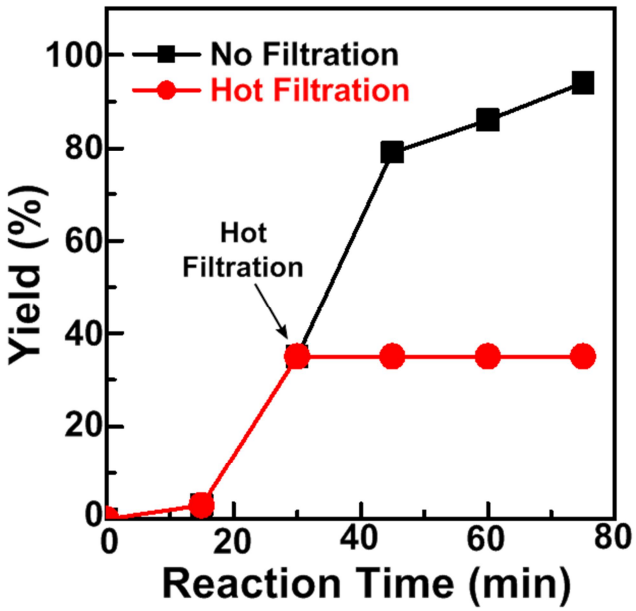

Figure II-7. Yields of the Suzuki coupling reactions between iodobenzene and phenylboronic acid with and without hot-filtration (the reaction was catalyzed by Pd-IPG and performed under the optimized conditions).

Moreover, the STEM-EDX analysis of Pd-IPG after 10 repeated reaction cycles supported the hot-filtration results. Based upon these findings and our previous mechanistic studies for Pd-Fe_3O_4 nanocrystal catalyst system,[79] the Suzuki coupling reaction mechanism in this system with the use of Pd-IPG may be suggested as follows: Presumably the Pd species from the Pd-IPG catalyst system goes into the catalytic cycle of oxidative addition, transmetallation followed by reductive elimination and this active Pd catalyst could be trapped alongside the ionic polymer species, thus allowing for excellent recovery and minimal loss of the catalyst. The observed catalytic efficiency, superior reusability, and chemical stability of the Pd-IPG catalyst suggest that the catalyst could be an effective candidate for constructing biaryl units from C-C coupling reactions including Suzuki, Heck, and Sonogashira coupling reactions.

2.3. Conclusions

Pd-IPG nanocomposite catalysts were successfully synthesized through facile one-pot and one-shot-injection methods using benzoic acid as a structure-directing agent. The optimized reaction conditions utilizing Pd-IPG as a catalyst for the Suzuki coupling reaction between iodobenzene and phenylboronic acid exhibited excessively high yield (99%) and catalytic activity (TOF: 990 h^{-1}), recording ~16-fold higher TOF than that of Pd-rGO (TOF: 61.3 h^{-1}). This increased reactivity indicates that the presence of ionic polymers on the rGO support can lead to highly facile Suzuki coupling reactions because of great dispersion stability, better accessibility and diffusion of the substrates to the nearby Pd species and the strong cohesion with the reacting species. However, the reactivity was relatively degraded in the case of the reaction with bromide-mediated substrates. The Pd-IPG catalyst exhibited excellent recyclability with consistently high yields (>96 %) and almost unchanged morphology and Pd content of the catalyst even after 10 repeated use. Plausible reasons for the retention of Pd content without noticeable leaching may include the capture of Pd species by nearby ionic polymer groups. These findings suggest that Pd NPs-based catalysts with ionic polymer-doped graphene could be an excellent breakthrough for solving the problems of homogeneous catalysts as well as to significantly enhance the catalytic activity of catalysts based on Pd NPs and carbon supports.

2.4. Experimental

2.4.1. Synthesis of pyrene-functionalized PDMAEMA-b-PPEGMEMA ionic block polymer.

According to the typical atom transfer radical polymerization (ATRP) technique, the reagents CuCl (0.75 mmol, 77.7 mg), dNbpy (1.5 mmol, 0.64 mg), 2-(dimethylamino)ethyl methacrylate (DMAEMA) (18.8 mmol, 3.2 mL), anisole (10.5 mL), and a solution of 2-EBP (0.6 mmol, 0.9 mL, 700 mM in toluene) were sequentially added. The reaction mixture was stirred at 80 ^{o}C for 14 h, and around 97% conversion was observed. According to an in-situ process, poly(ethylene glycol) methyl ether methacrylate (PEGMEMA) monomer (18.8 mmol, 8.97 mL) was sequentially injected into the unpurified PDMAEMA solution and then the reaction was stirred for 16 h, yielding around 97% conversion. For its purification, the reaction solution was quenched upon cooling to -78 ^{o}C immediately using liquid nitrogen and then diluted with 30 mL of THF. This solution was passed through an aluminium oxide column with extra THF. After concentration of collected solution under reduced pressure, the solution was dropped into hexane. Thereafter, precipitates were separated from the liquid by a decantation process. The obtained precipitates were dissolved in THF and then the precipitation process was repeated 3 cycles. Finally obtained PDMAEMA-*b*-PPEGMEMA block copolymer was dried at RT for 48 h, yielding MW: 19k and MWD: 1.09. The obtained resulting product was functionalized with an addition of pyrene moiety into PDMAEMA block through the Menshutkin reaction. For this, 0.5 g of PDMAEMA-*b*-PPEGMEMA was dissolved in DMF (9.6 mL) and then 1-(bromomethyl)pyrene (0.39 mM, 0.116g) was added to the prepared solution. The reaction was completed after heating the reaction mixture at 60 ^{o}C for 24 h, yielding

pyrene-functionalized PDMAEMA-b-PPEGMEMA ionic block polymer with 14 pyrene units per chain in over 95% yield. Purification was performed by precipitation in 200 mL of hexane after removal of DMF and then dissolving in THF. The resulting product, pyrene-functionalized poly(dimethylaminoethyl methacrylate)-*b*-poly[(ethylene glycol) methyl ether methacrylate] (Py-PDMAEMA-b-PPEGMEMA) ionic block copolymers, were dried at RT for 48 h under reduced pressure. ^{1}H NMR (300MHz, $CDCl_3$, δ) (ppm): 7.9-8.4 (broad, pyrene), 5.2-5.7 (broad, 2H, NCH_2pyrene), 4.2-4.8 (broad, 2H, $OCH_2CH_2N(CH_3)_2(CH_2)_2$Pyrene), 4 (t, 2H, $OCH_2CH_2N(CH_3)_2$), 3.4-3.8 (broad, 4H, CH_2CH_2O) 3.36 (s, 3H, $CH_2CH_2OCH_3$), 2.5 (t, 2H, $OCH_2CH_2N(CH_3)_2$), 2.3 (s, 6H, $OCH_2CH_2N(CH_3)_2$), 1.6-2.1 (broad, 2H, CH_2CCH_3 backbone), 0.7-1.3 (broad, 3H, CH_2CCH_3 backbone).

2.4.2. *Synthesis of graphene oxide (GO).*

GO dispersion was prepared by the oxidative exfoliation of graphite powder (Sigma Aldrich, Graphite flakes), following modified Hummer's method. Briefly, 1 g of graphite powder was oxygenated in 40 mL H_2SO_4, while stirring for 15 min, which was followed by slow adding of 3.5 g potassium permanganate under an ice bath. The mixture was then continuously stirred for 24 h at 35 °C. After completion oxygenation, the excess amount of deionized water and 35% H_2O_2 were added to the mixture. The obtained yellow mixture was thoroughly filter washed with 1 M HCl solution and deionized water and re-dispersed in 1 L of deionized water. The monolayer exfoliation was achieved by the sonication of the washed GO dispersion in water bath ultrasonicator. Subsequent purification was performed by dialysis and centrifugation to remove ionic impurities and unexfoliated graphite oxides. A predetermined amount of the concentrated dispersion was

diluted in deionized water to prepare the GO dispersions with a desired composition.

2.4.3. *Synthesis of reduced graphene oxide (rGO).*

Reduced graphene oxide (rGO) was synthesized through a high temperature thermal annealing of freeze-dried GO in temperature controlled furnace. First, the freeze-dried GO was placed in quartz tube and placed into the furnace at 100 ^{o}C for 1 hr. Then, the furnace temperature was increased with the rate of 10 ^{o}C/min up to 1000 ^{o}C and kept for 1 hour. Thereafter, the furnace temperature was allowed to cool down to room temperature and rGO powder was collected from quartz tube. All the reactions were performed under continuous flow of Ar gas.

2.4.4. Synthesis of Pd-IPG nanocomposite catalysts

Pyrene functionalized poly(dimethylaminoethyl methacrylate)-*b*-poly[(ethylene glycol) methyl ether methacrylate] (Py-PDMAEMA-*b*-PPEGMEMA), quaternary ammonium cation containing ionic polymer-doped reduced graphene oxide (0.4 mg, IPG), prepared following our previous report, was dispersed in 15 mL DMF by sonication for 10 min.[31] Benzoic Acid (7.3 mg, Sigma-Aldrich, >99.5%) was sequentially added to the IPG solution, and the mixture was gently sonicated for 5 min. Thereafter, this solution was placed on an ice bath and agitated for 5 min. After the foregoing procedure, aq Na_2PdCl_4 solution (2 mL, 20 mM in water, Sigma-Aldrich, 99.995%) was injected to the prepared solution, and the mixture was strongly agitated in an ice bath for 10 sec. The reaction was retained at 130℃ for 30 min. Thereafter, the reaction solution was stirred in an ice bath for 10 min. The crude product was purified by centrifugation 3 times using an ethanol and acetone (2:1) mixture. The obtained precipitates were dispersed in 100 mL of THF by

sonication for 10 min and the resulting products were obtained by filtration under reduced pressure. The filtered powder was dried at room temperature under reduced pressure for 24 h.

2.4.5. Evaluation of catalytic activity of the Pd-IPG nanocomposite catalysts for Suzuki coupling reactions

Suzuki coupling reactions using the Pd-IPG were performed at 60 ^{o}C after preparing the reaction solution including arylboronic acid (0.12 mmol), aryl iodide (0.1 mmol), NaOH (0.20 mmol), anisole (0.1 mmol), Pd-IPG (0.1 mol%) in ethanol/water (1:1 v/v, 0.8 mL). The reaction yield was monitored by GC analysis, where a small amount of the crude solution was taken and applied to GC analysis at the predetermined time after simple filtration. The completed reaction mixture was cooled to room temperature. Thereafter, Pd-IPG was separated from the reaction by facile filtration and the filtrate was extracted with ethyl acetate. The obtained organic part was used for GC analysis. The reaction yield was calculated by using anisole as an internal standard.

2.4.6. Recyclability test of the Pd-IPG nanocomposite catalysts

Suzuki coupling reactions of phenylboronic acid (0.60 mmol) with iodobenzene (0.50 mmol) were performed using Pd-IPG (0.1 mol%), NaOH (1.0 mmol), and anisole (0.50 mmol) in ethanol/water (1:1 v/v, 4.0 mL). After dilution of the crude reaction solution with ethyl acetate, the solution was filtered to separate the Pd-IPG. The acquired Pd-IPG was redispersed in ethanol/water (1:1 v/v, 4.0 mL) for the next reaction and the organic part was used for GC analysis to calculate the reaction yield after extraction with ethyl acetate. The foregoing procedure was

repeated up to ten times to investigate the recyclability of Pd-IPG.

2.4.7. Hot-filtration test of the Pd-IPG nanocomposite catalysts

For hot-filtration test, a Suzuki coupling reaction between phenylboronic acid (0.24 mmol) and iodobenzene (0.20 mmol) was conducted under optimized conditions. The reaction was maintained for 30 min and then a half volume of the reaction solution was taken and filtered while hot. Thereafter, the reaction yields of the hot filtrate and an unfiltered half of the solution were monitored through GC analysis after sampling small amounts of the reaction solutions at the predetermined time.

2.4.8. Characterizations

Scanning transmission electron microscopy (STEM) was applied for analysis of elemental mapping and energy dispersive X-ray (EDX) (FEI Talos F200X, maximum accelerating voltage of 200 kV) analyses. X-ray photoelectron spectroscopy (XPS) analysis was performed under reduced pressure using an X-ray photoelectron spectrometer (X-TOOL, ULVAC-PHI) with a monochromatic AlKα source. The phase was identified by matching each characteristic peak with the JCPDS files. Synthesized graphene supports were characterized using Raman spectrometer (LabRam ARAMIS IR2, Horiba, Japan). X-ray diffraction patterns were acquired on a Rigaku diffractometer (Rigaku Smart Lab, Rigaku Co., Japan) operated at 45 kV and 40 mA with CuKα radiation (λ = 1.5406 A°) using a diffracted beam monochromator. Data were collected between 2θ = 5° and 100° at 0.01° intervals. Evaluation of yields and catalytic activity was determined by gas chromatography (GC, Hewlett Packard 5890) analysis. ^{1}H and ^{13}C NMR spectra were obtained on Agilent MR DD2 (400 MHz) spectrophotometer.

Chapter 3.

A Novel Design Strategy for Blue Thermally Activated Delayed Fluorescence Molecules: Donor-Acceptor Interlocking by C-C Bonds

*Part of this thesis was published in Nanomaterials, **2019**, 9, 1735.

3.1. Introduction

OLED's have attracted much attention due to its application to display devices. Commercial OLED devices are already widely used in the market. However, because of its low efficiency and other limitations, continuous effort has been concentrated on the development of efficient and stable devices employing the OLED principle. In this regard, TADF emitters allow an internal quantum efficiency theoretically up to 100% by harvesting both singlet and triplet excitons via reverse intersystem crossing (RISC). Thus, TADF technology has attracted significant attention.[80-81]

To facilitate the RISC process in the TADF phenomenon, it is necessary to have a small singlet-triplet energy gap (ΔE_{ST}) between the lowest singlet energy and triplet energy in excited states, which is typically laid less than 0.37 eV. [82-86] The backbones of the TADF emitters are made up of an electron-donating and -accepting moieties for spatial separation of highest occupied molecular orbital (HOMO) and lowest occupied molecular orbital (LUMO) distributions. The use of electron-donating and -accepting building blocks generates a charge transfer structure by localizing HOMO and LUMO orbitals. This localization can be favored by increasing the twist angle between the donor and acceptor moiety. As a result, weak overlap of HOMO and LUMO tends to lead to small ΔE_{ST}. However, a minimal overlap of the orbitals is necessary for high quantum yields to take place, so a trade-off between small ΔE_{ST} and overlap has to be found.[87-89]

Because generally used donor units contain aniline- and carbazole-type electron-rich functional groups, the bridge between the donor and acceptor moiety is usually interlocked by a carbon-nitrogen (C-N) bond.[90-99] The carbazole type donor moiety can be readily introduced

through a C-N bond connection to the main building block, typically via nucleophilic aromatic substitution reactions (S_NAr). The average bond dissociation energy of a C-N bond (305 KJ/mol) is lower than that of carbon-carbon (C-C) bonds (347 KJ/mol), therefore the C-N bonds connected between the donor and acceptor units are considered susceptible to the degradation of TADF emitters during the photoluminescence process. In particular, deep blue emitters have a large excitation energy, approximately 3.0 eV.[81] To alleviate possible degradation of the deep blue TADF materials, a more stable junction between the donor and acceptor groups is deemed more desirable than the C-N bond connection.

Table III-1. The performances of the latest TADF emitters reported in the literature since 2017.

Entry	Compound	Performance	Group (Year)	Ref.
1	Sf-3Cz	15% EQE at 100 cd/m^2 CIE (0.16, 0.14)	L-S. Liao group (2018)	100
2	G2	no EQE CIE (0.15, 0.12)	Li Jie group (2017)	101
3	3DpYM-pDTC	20% EQE at 500 cd/m^2 CIE (0.14, 0.18)	C.-H. Cheng group (2017)	102
4	TXAZ	16% EQEmax CIE (0.15, 0.13)	J.-J. Kim group (2019)	103
5	FATA	11% EQEmax CIE (0.15, 0.13)	H. Kaji group (2018)	104
6	Ac3MHPM	10% EQE at 100 cd/m^2 CIE (0.16, 0.15)	J. Kido group (2017)	105
7	CNICtCz	10% EQE at 100 cd/m^2 CIE (0.14, 0.13)	J. Y. Lee group (2017)	106
8	DCzBN3	10% EQE at 100 cd/m^2 CIE (0.15, 0.06)	C. Adachi group (2018)	107
9	TN4T-PCZ	20% EQE at 100 cd/m^2 CIE (0.16, 0.03)	H. Meng group (2018)	108

The latest developments on TADF emitters reported in the literature since 2017 are collected in Table III-1. These are focused on efficient devices (external quantum efficiency; EQE >10%) with blue color (color coordinates <0.16). Most of the collected articles place their main focus on achieving deep blue color. While these deep blue TADF emitters have high EQE values, they suffer from high roll-off. Very few data are provided on device stability.[82-90]

Herein, we demonstrate that a novel molecular design, employing a C-C bond interlocking of donor and acceptor moieties, can lead to the stability improvement of blue TADF emitters. Our modelling studies on a series of C-C bonding TADF emitters suggested lower calculated ΔE_{ST} values, which was one of the most important factors for increased TADF phenomenon over those of the general C-N bond blue TADF emitters (e.g. the ΔE_{ST} value of **BMK-T138** and **CPT2** were 0.10 and 0.32 eV, respectively).[98,99] Therefore we designed and synthesized new TADF emitters having interlocked acceptor units on their carbazole or dibenzofuran backbone structures via C-C bond connections. Between the two backbone structures, those containing the dibenzofuran moiety were characterized by short delayed fluorescence lifetimes (τ_{DF}), owing to high kRISC values. Thus, compounds equipped with the dibenzofuran core structure were expected to be even more stable than those with the carbazole structure. Newly designed TADF emitters consist of an interlocked acceptor at the central core, coupled with a carbazole or dibenzofuran donor in the backbone structure for a small ΔE_{ST}. Restricted rotation of the central core via a C-C bonding architecture leads to a large dihedral angle between the donor and acceptor because of the large steric hindrance, affecting the short delayed fluorescence lifetime (τ_{DF}).[109]

3.2. Results and Discussion

The new TADF molecular design concept was based on interlocking an acceptor through a C-C bond on the carbazole or dibenzofuran backbone structures to increase the stability of TADF emitters. We selected totally six compounds among candidate structures suggested from virtual simulation screening, which research was collaborated with Samsung Advanced Institute of Technology (SAIT). Four compounds (**BMK-T236, 237, 317 and 318**) were synthesized and the others (**BMK-T138 and 139**) were provided from SAIT as reference compounds for comparing physical properties.

First of all, we compared three carbazole backbone compounds (**BMK-T138, 236 and 237**) by controlling proper donor and acceptor composition. Diphenyltriazine and isophthalonitrile attached at the 2-position of the carbazole backbone structure were selected as an acceptor unit, and a carbzole and di-*tert*-butylcarbazole at the 3-position of the carbazole backbone structure were chosen as an additional donor unit. The close-in location of the acceptor and additional donor was chosen for the installment of a proper twist angle between the two units. The twist angle of the emitter molecules affects the degree of HOMO-LUMO overlap.

The SAIT's procedure for the synthesis of **BMK-T138** and **BMK-T139** was also provided in **Sheme III-1**. As shown in **Scheme III-1**, 3-fluoro-9H-carbazole **(1)** was selected as a common starting material for the synthesis of **BMK-T138** and **BMK-T139**. After phenylation on the carbazole nitrogen, a boronic acid unit was introduced at the carbazole ring to yield a mixture of isomers **3a** and **3b** in a 5:1 ratio. Suzuki–Miyaura cross-coupling reaction of the resulting boronic acid derivative with a triazine derivative **4** in the presence of a Pd catalyst provided a

mixture of regioisomers, 2-(4,6-diphenyl-1,3,5-triazin-2-yl)-3-fluoro-9-phenyl-9H-carbazole **(5a)** and 3-fluoro-4-(4,6-diphenyl-1,3,5-triazin-2-yl)-9-phenyl-9H-carbazole **(5b)**, which were readily separated via column chromatography. The two regioisomers, **5a** and **5b**, were obtained in 36 and 7% yields, respectively. Finally, S_NAr reactions of **5a** and **5b** with a carbazole unit provided the target molecules, **BMK-T138** and **BMK-T139**, in 49 and 85% yields, respectively.

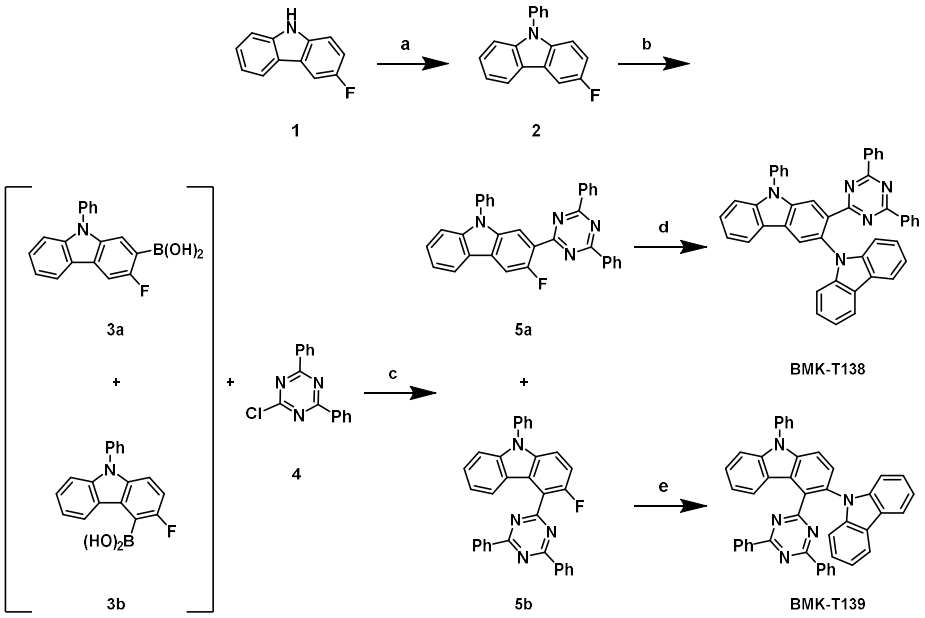

Scheme III-1. SAIT's synthetic routes of **BMK-T138** and **BMK-T139**. a) iodobenzene, K_3PO_4, CuI, *N*,*N*'-diacetylcyclohexane-1,2-diamine, dioxane, 80 ^oC; 86%; b) triisopropyl borate, lithium 2,2,6,6-tetramethylpiperidide, tetrahydrofuran (THF), -60 ^oC, then 1 N HCl, r.t.; c) $Pd(OAc)_2$, tri-o-tolyphosphine, H_2O, THF, 80 ^oC, 36% yield from 2 steps; d) Carbazole, tBuOK, *N*,*N*-dimethylformamide (DMF), 160 ^oC, 49%; e) Carbazole, tBuOK, DMF, 160 ^oC, 85%.

To improve difficulty of regio-isomer separation in SAIT's synthetic route, the new synthetic route was needed. As shown in **Scheme III-2**, the choice of 2-bromo-3-fluoro-*9*-phenyl-9*H*-carbazole **(9)** as a key intermediate material secured regio-selective introduction of the boronic acid moiety. From *N*-(4-bromo-5-fluoro-[1,1'-biphenyl]-2-yl)acetamide **(6)**, the carbazole backbone unit **(7)** was synthesized via intramolecular C-H bond amination with the use of (diacetoxy)iodobenzne as an oxidant according to Jonas Lategahn's protocol in the literature (*Angew. Chem. Int. Ed.* **2011**, *50*, 8605-8608).[110] After deacetylation followed by phenylation of the carbazole nitrogen, regio-selective borylation at the 2-position of the carbazole was successfully carried out.[111, 112] Suzuki-Miyaura cross-coupling reaction of the resulting boronic acid derivative **(3a)** was performed with an isophthalonitrile derivative **(10)** with the use of a Pd catalyst in the same manner as **Scheme III-1**. However, synthesis of **BMK-T236** through S_NAr reaction has not been successful due to the steric hindrance of the reacting species and the undesired hydrolysis **(12,13)** of the nitrile functionality under harsh reaction conditions.

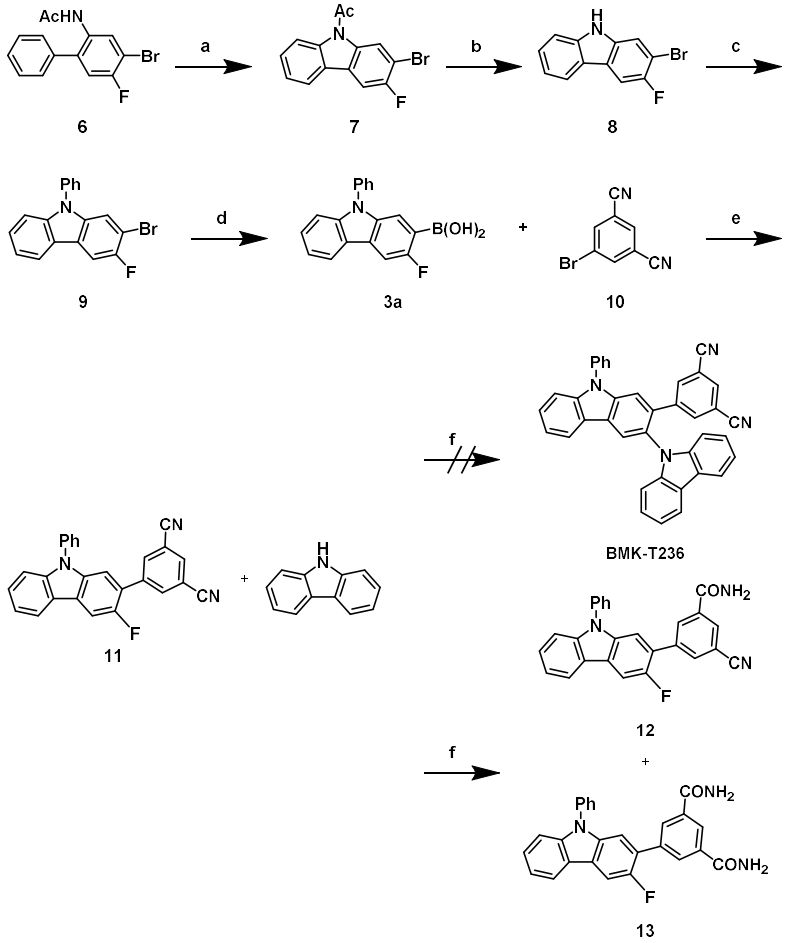

Scheme III-2. First synthetic routes of **BMK-T236**. a) (diacetoxy)iodobenzene, 1,1,1,3,3,3-hexafluoro-2-propanol (HFIP), r.t. 76%; b) KOH, MeOH, reflux; c) iodobenzene, K_3PO_4, CuI, diacetylcyclohexane, dioxane, 80 °C, 80% yield from 2 steps; d) trimethyl borate, n-BuLi, THF, -78 °C, then 2 N HCl, r.t., 34%; e) $Pd(PPh_3)_4$, 1 M K_2CO_3 in H_2O, THF, 80 °C, 17%; f) base, polar solvets, 160 °C.

In order to optimize the reaction conditions for the S_NAr reaction without undesired hydrolysis of the nitrile functionality, reaction condition screening was proceeded with various bases, solvents and temperature control (**Table III-2)**. The reaction was first screened with NaH, Cs_2CO_3, CsF, K^tOBu, and K_2CO_3 in DMF solution at 160°C. Various polar solvents were also screened with THF, DMF, dimethyl sulfoxide (DMSO), and *N,N*-dimethyl acetamide (DMA) at same

temperature. Unfortunately, the high reaction temperature over the 160°C caused the undesired hydrolysis of the nitrile functionality. Meanwhile, in case of other reaction temperature lower than 120°C, any reaction was not occurred.

Table III-2. Optimization of the reaction conditions for S_NAr reaction

Entry	Base	Solvent	Temperature (°C)	Result
1	Cs_2CO_3	DMF	160	Hydrolysis
2	CsF	DMF	160	Hydrolysis
3	K^tOBu	DMF	160	Hydrolysis
4	K_2CO_3	DMF	160	Hydrolysis
5	NaH	DMF	160	Hydrolysis
6	NaH	DMA	160	Hydrolysis
7	NaH	DMSO	160	Hydrolysis
8	NaH	THF	160	Hydrolysis
9	NaH	DMF	120	No reaction

Therefore, a new synthetic scheme was devised, which would allow the introduction of the carbazole derivative before an acceptor unit. As shown in **Scheme III-3**, the choice of 2-bromo-3-fluoro-*9*-phenyl-9*H*-carbazole **(9)** as a key intermediate material secured unequivocal introduction of the boronic acid moiety after early introduction of the carbazole unit, thus eliminating the undesired hydrolysis problem raised in **Scheme III-2.** After the S_NAr reaction at 3-position of carbazole backbone followed by borylation at 2-position of them, Suzuki-Miyaura cross-coupling reaction was finally carried out with an isophthalonitrile derivative **(10)**.

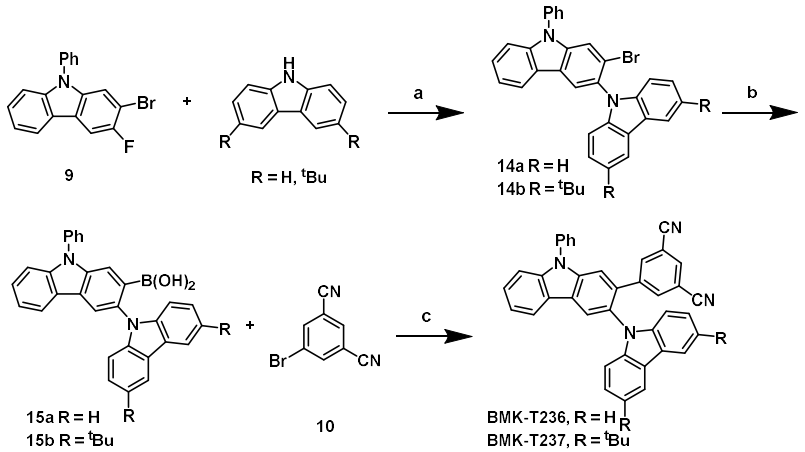

Scheme III-3. Revised synthetic routes of **BMK-T236** and **BMK-T237**. a) NaH, *N*,*N*-dimethylacetamide (DMA), 160°C, **14a** = 36%, **14b** = 22%; b) trimethyl borate, n-BuLi, THF, -78 °C , then 2 N HCl, r.t., **15a** = 48%, **15b** = 42%; c) $Pd(PPh_3)_4$, 1 M K_2CO_3 in H_2O, THF, 80 °C, **BMK-T236** = 45%, **BMK-T237** = 69%.

Our emitter design was guided by quantum chemical consideration using time-dependent density functional theory (TD-DFT) calculations, which provided estimates of the ΔE_{ST} for the donor-acceptor based emitters. We performed TD-DFT calculations on ground state geometries using the B3LYP[113] functional and the 6-31G* basis set in gas phase. Excited-state geometries and energies were derived by TD-DFT at the MPW1B95[114]/6-31G(d,p) level of theory. The RISC rate, k_{RISC}, was computed following Fermi Golden rule[115] and Marcus theory[116, 117]:

$$k_{RISC} = \frac{2\pi}{\hbar}|\langle S_1|H_{SO}|T_1\rangle|^2\sqrt{\frac{1}{4\pi k_B T\lambda_S}}exp\left[-\frac{(\Delta E_{ST}+\lambda_S)^2}{4\lambda_S k_B T}\right],$$

where $|\langle S_1|H_{SO}|T_1\rangle|$ is the Spin-Orbit Coupling (SOC) matrix element between the S1 and T1 states. k_B is Boltzmann constant, and T is temperature, which was set to 298 K. ΔE_{ST} denotes the energy difference between the S_1 and T_1 states, and λ_S represents the reorganization energy which can be formulated as

$$\lambda_S = E_{S1}(T_1\ geometry) - E_{S1}(S_1\ geometry),$$

All DFT and TD-DFT computations were performed using the Gaussian 09 package,[118] and the SOC calculations were performed using ADF package.[119]

Base on this calculation, the simulation data of the three TADF emitters are tabulated in **Table III-3**. Among the three compounds synthesized, **BMK-T138** was predicted to have a proper emission wavelength of 461 nm for deep blue color and a low energy gap (ΔE_{ST}) of 0.10 eV for intersystem crossing. Therefore, the three emitters were tested for photophysical properties in toluene under N_2 as shown in **Table III-4**.

Table III-3. Density functional theory (DFT)-calculation data of **BMK-T138, BMK-T236,** and **BMK-T237**

Name	TD-DFT[a]					
	HOMO (eV)	LUMO (eV)	S1 (eV)	T1 (eV)	ΔE_{ST} (eV)	Spectrum (nm)
BMK-T138	−5.157	−1.795	2.77	2.67	0.10	461
BMK-T236	−5.520	−1.950	2.99	2.93	0.06	423
BMK-T237	−5.310	−1.940	2.82	2.79	0.03	451

[a] The geometry in S_0 was optimized by DFT calculation.

Although **BMK-T138** was predicted to exhibit a proper blue emission spectrum, its photoluminescence (PL) peak in toluene solution under N_2 appeared at 478 nm, which was a little bit red-shifted from the predicted value. Meanwhile PL peaks of **BMK-T236** and **BMK-T237** exhibited deep blue emission spectra of 435 nm and 448 nm in solution, respectively as shown in **Table III-4**.

All of the TADF emitters possessing C-C bond connections exhibited narrow full width at half-maximum (fwhm) of 59-66 nm. Furthermore, its maximum ΔE_{ST} value was only 0.21 eV, which is sufficient to generate delayed fluorescence phenomenon. But the τ_{DF} value of

BMK-T138 was 163 μs and the emission spectra of it peaked at 478 nm. This results were somewhat disappointing. Both **BMK-T236** and **BMK-T237**, on the other hand, had shorter τ_{DF} values than that of **BMK-T138** (4.1 and 17.0 μs respectively). And **BMK-T236** and **BMK-T237** having isophthalonitrile functional group exhibited the blue-shifted PL peaks of 435 nm and 448 nm, respectively. Because isophthalonitrile functional group is weaker acceptor unit than diphenyl triazine functional group. However, the low PLQY values of them are attributed to the excessive energy stored in exciton states, which was also implied by the prominent blue-shifted phenomenon.

Table III-4. Photophysical properties of **BMK-T138, BMK-T236,** and **BMK-T237**

Name	Physical properties of TADF emitters[a]						
	PL (nm)	FWHM (nm)	E_S [b] (eV)	E_T [b] (eV)	ΔE_{ST} [c] (eV)	τ_{DF} (μs)	PLQY[d] (%)
BMK-T138	478	66	2.87	2.82	0.05	163	74
BMK-T236	435	59	3.12	2.90	0.21	4	14
BMK-T237	448	59	3.02	2.87	0.15	17	12

[a] Measured in toluene solution. [b] Energy of singlet and triplet estimated from onset of wavelength in toluene solution. [c] $\Delta E_{ST} = E_S - E_T$. [d] PLQY values estimated with DPEPO host.

To improve the limitation of previous research, we synthesized two more TADF emitters (**BMK-T317** and **BMK-T318**) having dibenzofuran backbone core structure among candidate emitters. Diphenyltriazine attached at the 2- or 4-position of the backbone structures was selected as an acceptor unit, and a carbzole moiety at the 3-position of the backbone structure was chosen as an additional donor unit. Finally, we compared four emitters (**BMK-T138, 139, 317,** and

318) and reference TADF emitter (**CPT2**) possessing C-N bond connections, which was reported in Adachi's study (*Adv. Mater.*, **2017**, *29*, 1702767.).[98]

For the construction of molecules containing a dibenzofuran moiety instead of a carbazole unit at the backbone structure, a synthetic pathway featuring 3-bromo-2-fluorodibenzo[*b*,*d*]furan **(16)** as a key intermediate molecule was adopted as shown in **Scheme III-4**. Compound **16** would secure regioselective introduction of the boronic acid moiety for the construction of **BMK-T317**, which called for adjoining triazole and carbazole units. Compound **16** was purchased from Medigen Co. and used without further purification. After introducting a carbazole unit at the 2-position of compound **16** via a S_NAr reaction, we converted the bromo group to the corresponding boronic acid **(18)** via borylation at the 3-bromo position, followed by hydrolysis. Suzuki-Miyaura cross-coupling reaction was finally carried out with a triazine derivative **4,** using a Pd catalyst in the same manner as shown in **Scheme III-1** to provide the desired compound, **BMK-T317**, at a 45% yield.

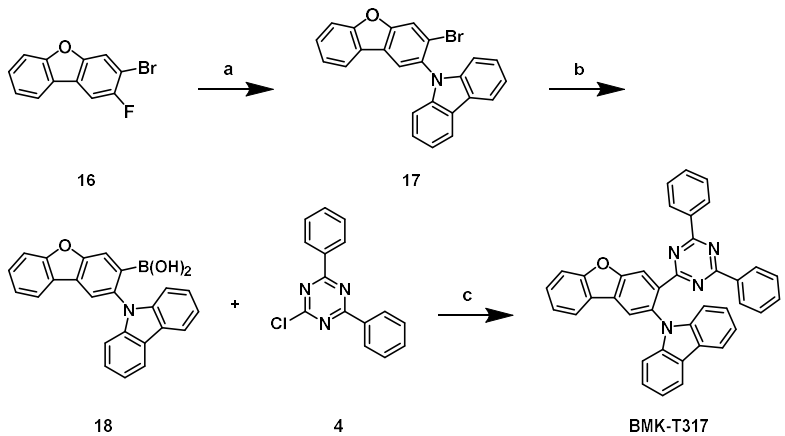

Scheme III-4. Synthetic routes of **BMK-T317**. a) Carbazole, NaH, DMA, 160 °C, 44%; b) trimethyl borate, n-BuLi, THF, -78 °C , then 2 N HCl, r.t., 51%; c) $Pd(PPh_3)_4$, 1 M K_2CO_3 in H_2O, THF, 80 °C, 45%.

For the synthesis of **BMK-T318**, a new synthetic pathway was devised, which allowed the introduction of a carbazole unit before a triazine one, as shown in **Scheme III-5**. The placement of the triazine unit in **BMK-T318** required compound **19** as a key intermediate. Compound **19** was also purchased from Medigen Co. and used without further purification. After introduction of the carbazole unit via the S_NAr reaction at the 2-position of the benzofuran backbone **19**, borylation was carried out at the 1-position for final Suzuki-Miyaura cross-coupling reaction with a triazine unit **4** in the same manner as shown in **Scheme III-4**.

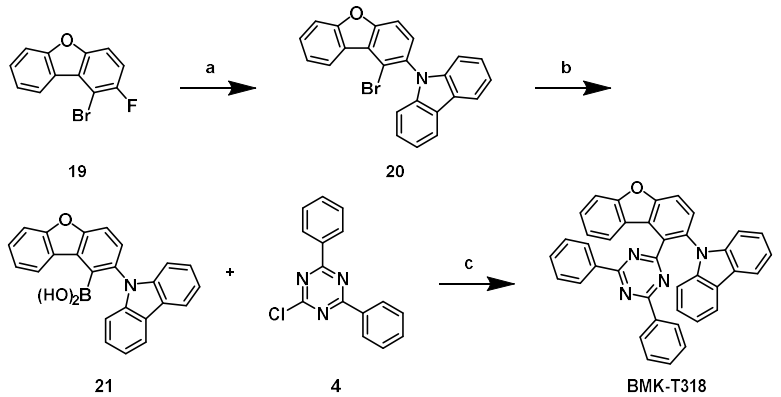

Scheme III-5. Synthetic routes of **BMK-T318**: a) Carbazole, NaH, DMA, 160 °C, 19%; b) trimethyl borate, n-BuLi, THF, -78 °C , then 2 N HCl, r.t., 55%; c) $Pd(PPh_3)_4$, 1 M K_2CO_3 in H_2O, THF, 80 °C, 45%.

The molecular orbital distributions of the emitter molecules are shown in **Figure III-1**. As can be expected from the molecular structures, the HOMOs were localized on the carbazole donor unit, whereas the LUMOs were dispersed over the diphenyl triazine acceptor unit. Strengths of donor and acceptor of the materials were affected by their

energy levels. Especially, the dibenzofuran core structure tended to be the weak electron transport (ET) type, compared to that of carbazole core structure. Therefore, the energy band of dibenzofuran based C-C bond molecules was lower than that of the carbazole based C-C bond molecules to maintain the energy band gap (**Table III-5**). This led to a lower HOMO energy level to balance the exciton in EML and to maintain blue emission. Four TADF emitters interlocking through the C-C bonds were equipped with greater dihedral angles, warranting lower ΔE_{ST} values than those of TADF emitters interlocking through C-N bonds.[120-126] In these molecules, hindered bond rotation caused by repulsive steric interaction not only partly interrupted the conjugation system, they also caused sectional deformation of both the linear and planar molecular structures, which inevitably affected the dihedral angle and emitter characteristics, such as ΔE_{ST} and oscillator strength (*f*). Therefore, the placement of a C-C bond on the donor-acceptor connection led to low efficiency roll-off for the newly designed material.

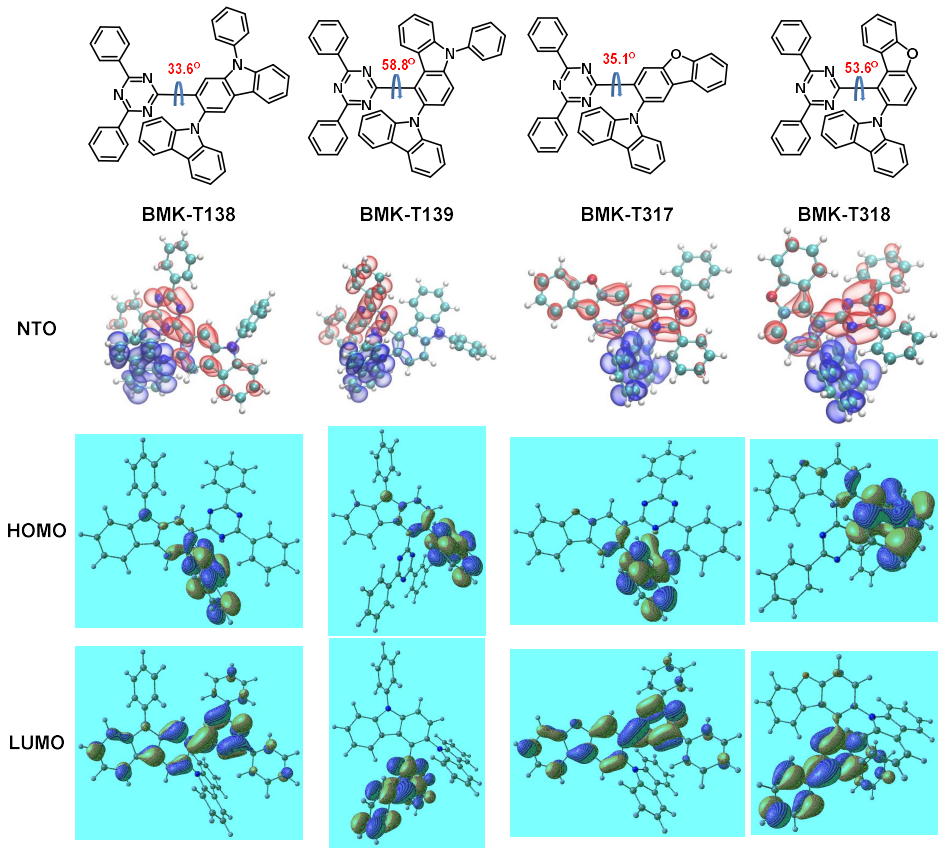

Figure III-1. Chemical structures and dihedral angle, natural transition orbital (NTO) hole (blue) and acceptor (red), and HOMO and LUMO orbital distributions.

As show in **Table III-5**, all four C-C bond TADF emitters were predicted to exhibit properly separated HOMOs and LUMOs as well as lower energy gaps (ΔE_{ST}) than 0.10 eV owing to the steric hindrance. It was confirmed that the ΔE_{ST} values of emitters having C-C bond connection (0.05 eV~0.10 eV) were three times smaller than those of emitters having C-N bond connection (0.32 eV), as reported in the case of compound **CPT2** in Adachi's study (*Adv. Mater.*, **2017**, *29*, 1702767.).[98] Due to the steric hindrance in our suggested structure, the dihedral angles of **BMK-T139** and **BMK-T318** were calculated to be 58.8° and 53.6°, respectively, which is much larger than those of C-N

bond connecting emitters (that of **CPT2** was 2.0 ^{o}). The ΔE_{ST} values were also reduced from those of C-N bond connecting emitters. On the other hand, the oscillator strength (*f*) value decreased significantly. Thus, the PL quantum yield (PLQY) was reduced by the influence of the reduced oscillator strength (*f*). To secure a desirable PLQY, we changed the core structure from carbazole to dibenzofuran.

Based on this calculation, emitters possessing the C-C bond connections were highly advantageous in terms of material stability, because their bonding energies increased. Among the four suggested compounds, both **BMK-T317** and **BMK-T318,** having a dibenzofuran backbone, were predicted to have much higher values of kRISC than those of **BMK-T138** and **BMK-T139**, having a carbazole backbone (**Table III-5**). This indicates that **BMK-T317** and **BMK-T318** had a short delayed fluorescence lifetime (τ_{DF}) with a high quantum yield.

Table III- 5. DFT-calculation data of the TADF emitters

Name	TD-DFT[a]							
	HOMO (eV)	LOUMO (eV)	*f*	S1 (eV)	T1 (eV)	ΔE_{ST} (eV)	kRISC (S^{-1})	dihedral angles (^{o})
BMK-T138	-5.16	-1.79	0.0067	2.77	2.67	0.10	8.17	33.6
BMK-T139	-5.16	-1.76	0.0043	2.86	2.81	0.05	2.99	58.8
BMK-T317	-5.30	-1.94	0.0051	2.76	2.70	0.06	5.25×10^5	35.1
BMK-T318	-5.31	-1.88	0.0063	2.84	2.78	0.06	4.49×10^5	53.6

[a] The geometry in S_0 was optimized by DFT calculation.

Optical absorption and PL spectra of the **BMK-T138**, **BMK-T139**, **BMK-T317**, and **BMK-T318** in dilute toluene solution (1×10^{-4} M) are shown in **Figures III-2**.

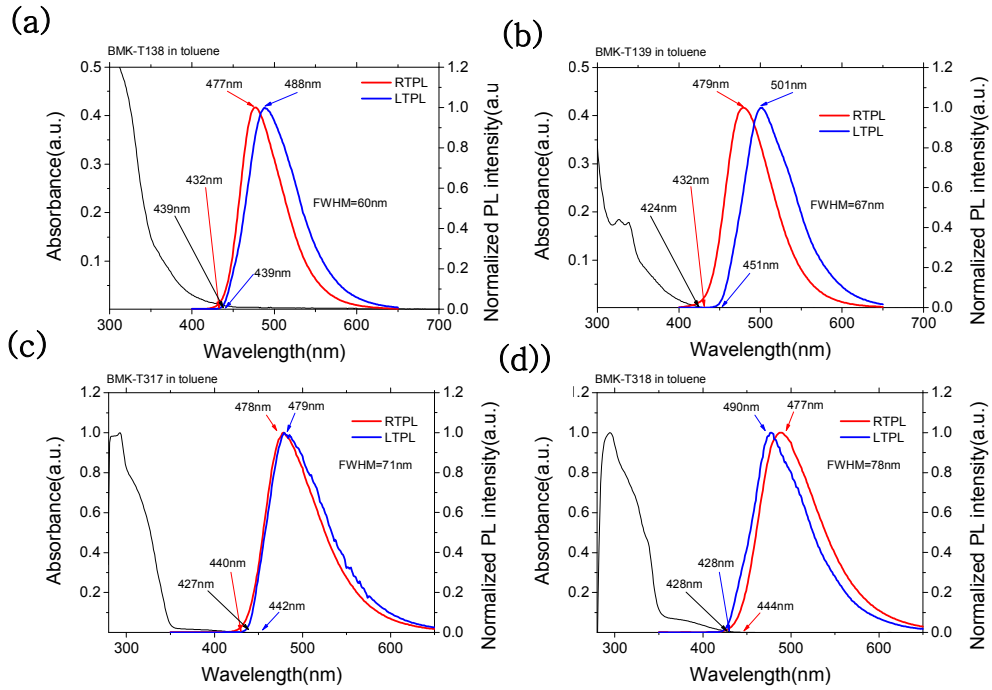

Figure III-2. Optical absorption and photoluminescence spectra of (a) **BMK-T138**, (b) **BMK-T139**, (C) **BMK-T317**, and (d) **BMK-T318**.

The E_S / E_T / ΔE_{ST} values of the **BMK-T138** and **BMK-T139** emitters were 2.87/2.82/0.05 and 2.87/2.75/0.12 eV, respectively, from the onset energy of the fluorescence and phosphorescence spectra. On the other hand, **BMK-T317** and **BMK-T318**, which used dibenzofuran-based emitters, exhibited smaller ΔE_{ST}, resulting from the E_S decrease and the E_T increase. As expected from the DFT-calculation, the singlet–triplet energy gaps of the emitters having C–C bonds were lower than that of the **CPT2** having a C-N bond (that of **CPT2** was 0.32 eV).[98]

The PLQY of **BMK-T138**, **BMK-T139**, **BMK-T 317**, and **BMK-**

T318 were found to be 74.1, 62.2, 69.7, and 73.7%, respectively. To improve the RISC yield while maintaining efficient PLQY of TADF emitters, we modified the core structure from a carbazole core to a dibenzofuran core.

Using the PLQY and transient PL data, the RISC yield was calculated for each emitter. Because the τ_{DF} values of the dibenzofuran-based TADF emitters decreased as expected in the calculation, the RISC yields of the dibenzofuran-based TADF emitters were shown to be higher than those of the carbazole-based TADF emitters (63.09 vs. 32.10). Additionally, large distortions of the donor from the acceptor linker increased the RISC yield with a reduced τ_{DF}.[127]

Table III-6. Photophysical properties in solution state of the TADF emitters

Name	Physical properties of TADF emitters							
	PL (nm)	FWHM (nm)	E_S (eV)[a]	E_T (eV)[a]	ΔE_{ST} (eV)[b]	PLQY[c] (%)	τ_{DF}[c] (μs)	kRISC yield (%)
BMK-T138	478	66	2.87	2.82	0.05	74	163	32.10
BMK-T139	480	72	2.87	2.75	0.12	62	147	50.80
BMK-T317	469	72	2.82	2.81	0.01	70	51	60.53
BMK-T318	466	75	2.79	2.90	-0.11	74	21	63.09

[a] Energy of singlet and triplet measured from onset of wavelength in toluene solution. [b] $\Delta E_{ST} = E_S - E_T$. [c] PLQY values were estimated with DPEPO host.

To compare the C-N and C-C bond skeleton molecules, device evaluation was conducted using a DPEPO host for **CPT2** and **BMK-T138** TADF emitters. Although **CPT2** exhibited short delayed fluorescence lifetimes (τ_{DF}) owing to its linear type TADF material, it showed very large efficiency roll-off because of the low bond dissociation energy of the C-N bond. Despite the long τ_{DF} value of **BMK-T138** (163 μs), the efficiency roll-off was significantly reduced because of the large PLQY and C-C bond stability. Furthermore, the maximum external quantum efficiency of **BMK-T138** was 19.6%, and the current efficiency was 40.53 cd/A, respectively.

To summarize, the performances of the device containing the C-C bond skeleton molecules appeared to have had the greatest effect on the stability of the material with a high PQLY (74%). Comparison of the physical properties of devices containing either a C-C bond emitter (**BMK-T138**) or a C-N bond emitter (**CPT2**) in a DPEPO host is summarized in **Table III-7**. The advantage of the emitter equipped with a C-C bond skeleton is increased overlap density of HOMO/LUMO distribution with greater dihedral angle between donor and acceptor (**Figure III-3**). By employing the dibenzofuran moiety without a phenyl linker as a core-structure and increasing overall rigidity and overlap density, we achieved short delayed fluorescence lifetimes (τ_{DF}). Moreover, the rigid structure was expected to result in reduced non-radiative mechanisms during light-emission.

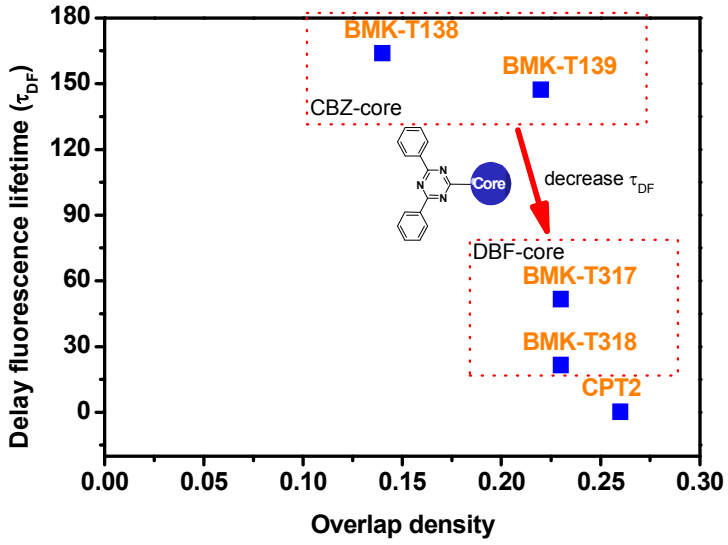

Figure III-3. Overlap density-delayed fluorescene lifetimes (τ_{DF}) data

Compared to the C-N bonding blue TADF emitter, those containing a C-C bond skeleton were expected to secure high efficiency with great stability of the device. As expected, **BMK-T138** TADF emitter with a long τ_{DF} significantly improved the external quantum efficiency for DPEPO host system. Thus, the device's material stability was an important factor for improving device performances. Therefore, we conducted additional photophysical experiments using the mCBP-CN host instead of DPEPO.[128] Although TADF emitters with a DPEPO host are characteristically adopted for device performance tests, we examined our emitters using the mCBP-CN host, focusing on optimizing the devices with suppressed efficiency roll-off.[129] DPEPO has the advantage of high efficiency with a wide band gap and high triplet energy to boost high-efficiency TADF devices. However, it is not suitable for device stability, because it is an unstable ET-type host material with low stability in EML. Because DPEPO has a quite

shallow LUMO for an ET-type host, all TADF emitters doped in DPEPO have deeper LUMOs than that of DPEPO. When all the TADF emitters with DPEPO host have a large band gap, both hole and electron carriers are likely to be trapped inside the transport layer. As a result, these trapped carriers expose dopant molecules under electrical stress, rendering the host-dopant system less efficient.

Because mCBP-CN has an ET-type character with deep LUMO, the emission layer composed of mCBP-CN host and TADF emitters showed better charge transport and balance than that of the DPEPO host. Therefore, we employed mCBP-CN, which is well fitted to our blue TADF emitters, having shallow LUMOs and HOMOs. Generally, the deep HOMO energy level causes a low hole injection rate in the hole-only devices (HOD). The TADF emitters having deep HOMO energy levels decreased the HOD strength. The four TADF molecules have similar tendencies, as shown in **Figure III-4**. Although the dibenzofuran core structure changed the energy level, it provided highly efficient performance by minimizing the charge balance in the emission layer for TADF devices. **Figure III-4** shows the correlation between the hole current and HOMO energy levels.

Table III-7. Device performance comparison between a C-C bond emitter (**BMK-T138**) and C-N bond emitter (**CPT2**) in the DPEPO host.

Name	EQE_{max} (%)	EQE[a] (%)	CE_{max} (Cd/A)	Roll-off (%)	EL (nm)	V_d (V)	Color Coordinates
CPT2	18.7	4.1	30.1	78.7	470	10.06	(0.16, 0.21)
BMK-T138	19.6	6.2	40.6	69.8	480	7.59	(0.16, 0.31)

[a] EQE at luminance of 500 cd/m^2

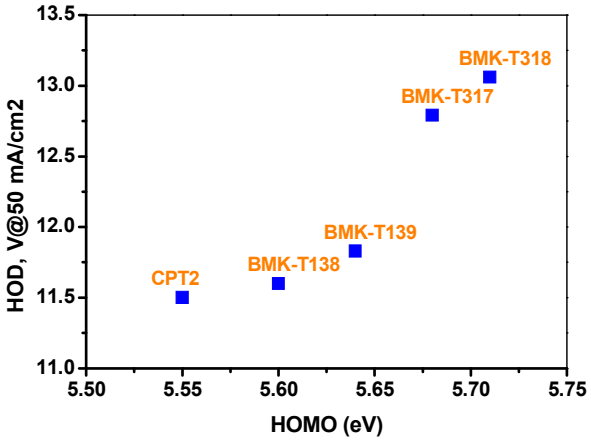

Figure III-4. hole current versus HOMO energy

The current density–voltage–luminance (J–V–L), and quantum efficiency–luminance–current efficiency characteristics of TADF devices with C-C bond skeleton emitters are shown in **Figure III-5**. TADF devices having dibenzofuran based emitters enhanced device performance (**BMK-T317** and **BMK-T318**) compared to those containing carbazole based emitters, as shown in **Figure III-4** and **Table III-8**. Dibenzofuran based devices showed a significantly reduced turn-on voltage of 4.68 and 4.36 V, exhibiting an increased current efficiency of 37.6 and 38.2 cd/A, respectively. On the other hand, carbazole based emitters showed high turn-on voltages (5.16 and 5.71 V) and current efficiencies of 33.8 and 21.8 cd/A, respectively. **BMK-T317** and **BMK-T318** also exhibited enhanced device performance, showing an EQE of 19.9 and 18.8%, respectively. In addition, the maximum luminance of **BMK-T318** was much lower than that of all TADF devices, presumably owing to the low current density. **BMK-T318** showed the lowest current density, and **BMK-T139** showed the highest. This can be correlated with the energy levels of the

core structures. The difference between the HOMO energy level of **BMK-T318** and that of the mCBP-CN host was only 0.39 eV, whereas the HOMO energy level difference between **BMK-T138** and mCBP-CN host was 0.50 eV. Therefore, **BMK-T318** is suitable for the blue TADF, because the energy barrier of **BMK-T318** was the lowest.

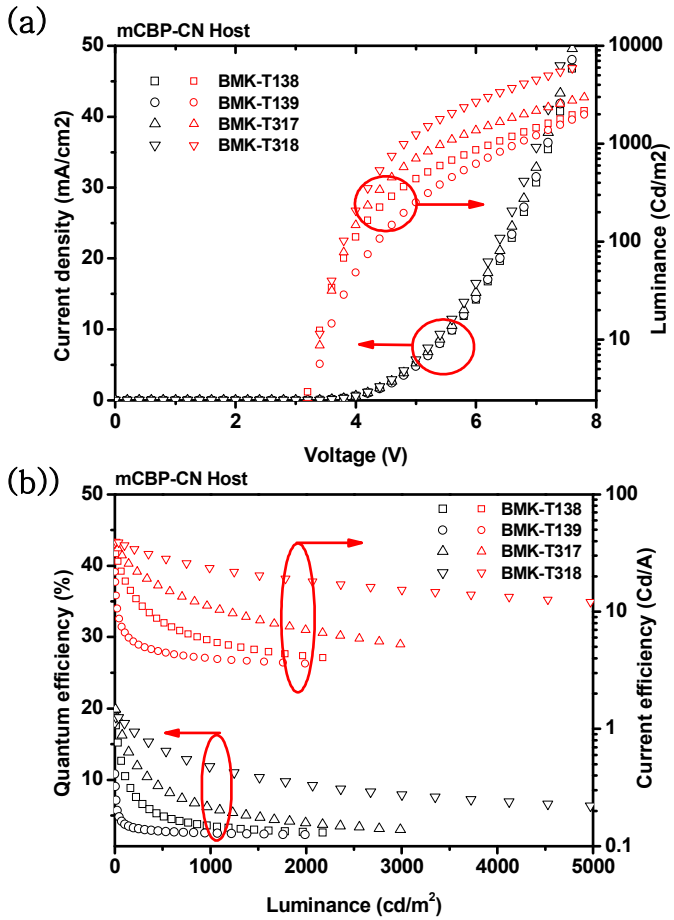

Figure III-5. BMK-T138, **BMK-T139**, **BMK-T317**, and **BMK-T318** TADF devices with an mCBP-CN (15%) host: (a) current (J–V–L); (b) external quantum efficiency and current efficiency versus current density curves.

Table III-8. Device performance of the TADF emitters having an mCBP-CN host

Name	EQE_{max} (%)	EQE^{a} (%)	CE_{max} (Cd/A)	Roll-off (%)	EL (nm)	J^{b} (mA/cm^2)	$V_d{}^{a}$ (V)	Color Coordinates
BMK-T138	18.8	5.0	33.9	75.8	473	8.17	5.16	(0.13, 0.24)
BMK-T139	10.8	2.8	21.8	79.3	473	11.08	5.71	(0.16, 0.32)
BMK-T317	19.9	8.8	37.6	57.3	475	3.15	4.68	(0.15, 0.23)
BMK-T318	18.8	14.3	38.2	26.7	481	1.75	4.36	(0.15, 0.27)

[a]EQE at luminance of 500 cd/m^2, [b]Current density (J) at driving voltage of 5V.

Dibenzofuran based materials also showed significantly enhanced efficiency roll-off because of the relatively low τ_{DF} values of **BMK-T317** and **BMK-T318** (51 and 21 μs, respectively), compared to the other τ_{DF} values of carbazole-based materials (**BMK-T138**, τ_{DF} = 163 μs and **BMK-T139**, τ_{DF} = 147 μs). In the case of **BMK-T138**, a large τ_{DF} value led to relatively poor efficiency roll-off than those of other C-C bond emitters. This implies that facilitating efficient host exciton transport from the recombination zone to the ground state with a high RISC yield is an important factor for securing TADF device stability. We note that RISC should be much faster than non-radioactive emission to the ground state to efficiently transfer energy from triplet to singlet. Therefore, device stability can be improved, and it can be advantageous in terms of device lifetime.

Electroluminescence (EL) spectra of all devices were investigated, as shown in **Table III-8**. The EL emission peaks were located at 473, 473, 475, and 481 nm, respectively (**Table III-8** and **Figure III-6**). The EL emission peaks of compounds possessing the dibenzofuran backbone group were a bit red-shifted from the PL peak values.

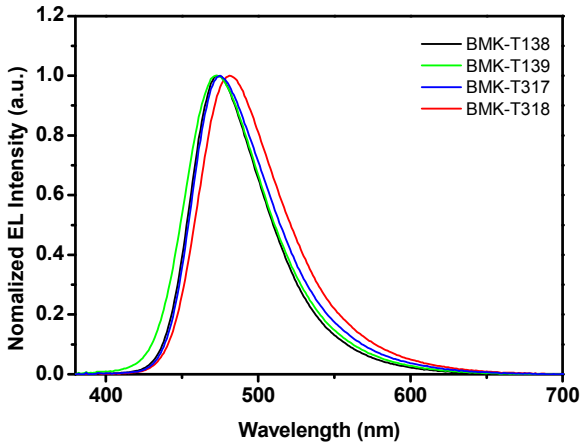

Figure III-6. The EL spectra of **BMK-T138**, **BMK-T139**, **BMK-T317**, and **BMK-T318** TADF devices.

3.3. Conclusions

A new design strategy of TADF emitters was proposed, entailing interlocking a donor with an acceptor through a C-C bond. The photophysical property data obtained from the synthesized compounds provided important insights on increasing stability of TADF materials during the photoluminescence process and the possibility of blue emission. A series of C-C bond TADF emitters were introduced, featuring large dihedral angle of the central core in adjacent donor and acceptor arrangement provoking large steric hindrance. These emitters exhibited properly separated HOMO–LUMO overlap and low ΔE_{ST} calculation values (<0.12 eV). The photophysical properties of C-C bonding TADF emitters were characterized by a narrow FWHM of 66 nm and a blue emission of 466 nm with a short fluorescence lifetime (τ_{DF}) of 21 μs in a solution state. The EL experimental results indicated a desirable EL peak of 473 nm and a high external quantum efficiency value of 19.9%. Especially clear reduction of the efficiency roll-off characteristics (26.7%) was observed in case of dibenzofuran core structure. It is evident that the efficiency roll-off affects the operational stability of TADF emitters. Therefore, the TADF emitters having a C–C bond connection have the potential to secure high efficiency and long life

3.4. Experimental

3.4.1. General information

Chemicals were purchased from Sigma–Aldrich Co., Tokyo Chemical Industry Co., and Wako Pure Chemical Industries Ltd., and used without further purification. The organic materials used in this study that did not have precedent syntheses were synthesized and characterized according to the methods described in the Supplementary Information. The ^{1}H and ^{13}C NMR-spectra were measured using an Agilent 400-MR DD2 magnetic resonance system (400 MHz) spectrophotometer or a Bruker ASCEND 500 (500 MHz) spectrophotometer. Chemical shifts were measured as parts per million (d values) from tetramethylsilane as an internal standard at probe temperature in CD_2Cl_2, $CDCl_3$, or DMSO-D_6 for neutral compounds. Coupling constants were provided in Hz, with the following spectral pattern designations: s, singlet; d, doublet; t, triplet; q, quartet; quint, quintet; m, multiplet; br, broad; app, apparent. The MLADI-TOF mass spectra were recorded using a Bruker Ultraflex III TOF/TOF 200 spectrometer. The ultraviolet–visible (UV-Vis) spectra were obtained by means of a Varian model UV-Vis near infrared spectrophotometer 5000, and the fluorescence spectra were measured on a HITACHI F7000 spectrometer for the solution states. The UV-Vis absorption and solution photoluminescence (PL) emission spectra of materials were obtained from a dilute toluene solution (1×10^{-5} M), whereas the solid PL spectra were obtained from thin films prepared by vacuum evaporation. Triplet energy values of the TADF materials were obtained from the photoluminescence spectra at 77 K using liquid N.

3.4.2. Synthesis and characterizations of compounds

1-(2-Bromo-3-fluoro-9H-carbazol-9-yl)ethan-1-one (7) : To a solution of biphney **6** (9.57 g, 31.1 mmol) in hexafluoroisopropanol (600 mL) was added phenyliodine diacetate (11.0 g, 34.2 mmol) at r.t.. The reaction mixture was stirred at r.t. for 8 hours. After finishing the reaction, the reaction mixture was concentrated under reduced pressure and extracted with methylene chloride. The organic layers were dried over anhydrous $MgSO_4$ and concentrated in *vacuo*.

There were two different purification method.

A. The resulting residue was purified by using flash column chromatography on silica-gel (EA:Hex=1:4) to afford carbazole **7** (28 mg, 76%). (in case of large scale experiment, it was difficult to purify from side product)

B. The resulting residue was filtered by using hexane. The filter-cake was several times repeated to precipitation until the clear carbazole **7** (5.86 g, 62%) was abtained.

^{1}H-NMR (400 MHz, $CDCl_3$, ppm) δ 8.63 (d, J = 6.0 Hz, 1H), 7.96 (d, J = 8.4 Hz, 1H), 7.89 (d, J = 7.6 Hz, 1H), 7.62 (d, J = 8.0 Hz, 1H), 7.52 (t, J = 8.0 Hz, 1H), 7.39 (t, J = 7.6 Hz,1H), 2.01 (s, 3H). ^{13}C-NMR (100 MHz, $CDCl_3$, ppm) δ 169.5, 155.8 (^{1}J = 242 Hz), 138.7, 135.2, 128.2, 126.5 (^{3}J = 8 Hz), 125.3, 123.8, 121.5, 120.4, 115.7, 108.0 (^{2}J = 23 Hz), 106.2 (^{2}J = 25 Hz), 27.6.

2-Bromo-3-fluoro-9H-carbazole (8) : To a solution of carbazole **7** (0.60 g, 1.96 mmol) in MeOH (15 mL) was added KOH at r.t.. The reaction mixture was stirred at 80 ^{o}C for 12 hours. The resulting

mixture was cooled and neutralized with sat. NH_4Cl solution, then extracted with methylene chloride. The organic layers were dried over anhydrous $MgSO_4$ and concentrated in *vacuo*. The resulting residue was purified by using flash column chromatography on silica-gel (EA:Hex=1:4) to afford carbazole **8** (28 mg, 76%).

^{1}H-NMR (400 MHz, DMSO, ppm) δ 11.4 (s, 1H), 8.15 (s, 1H), 7.78 (s, 1H), 7.52 (s, 1H), 7.44 (s, 1H), 7.18 (s, 1H). ^{13}C-NMR (100 MHz, DMSO, ppm) δ 152.5 (^1J = 232 Hz), 141.2, 137.0, 127.1, 122.8 (^3J = 9 Hz), 122.2 (^3J = 4 Hz), 121.3, 119.4, 115.0, 111.9, 107.5 (^2J = 25 Hz), 105.6 (^2J = 24 Hz).

2-Bromo-3-fluoro-9-phenyl-9H-carbazole (9) : To a solution of carbazole **8** (360 mg, 1.36 mmol) in dioxane (6 mL) was added K_3PO_4 (579 mg, 2.73 mmol), CuI (52 mg, 0.27 mmol), diaminocyclohexane (93 mg, 0.82 mmol) and iodobenzene (0.23 mL, 2.04 mmol) at r.t.. After stirring for 1 day at 90 °C, the resulting mixture was cooled and extracted with methylene chloride. The organic layers were dried over anhydrous $MgSO_4$ and concentrated in *vacuo*. The resulting residue was purified by using flash column chromatography on silica-gel (EA:Hex=1:4) to afford carbazole **9** (388 mg, 84%).

^{1}H-NMR (400 MHz, $CDCl_3$, ppm) δ 8.05 (d, J = 8.0 Hz, 1H), 7.83 (d, J = 8.4 Hz, 1H), 7.70-7.80 (m, 1H), 7.62 (t, J = 7.6 Hz, 2H), 7.51 (t, J = 8.4 Hz, 3H), 7.43 (d, J = 7.2 Hz, 1H), 7.36 (d, J = 8.0 Hz, 1H), 7.28 (t, J = 7.2 Hz,1H). ^{13}C-NMR (100 MHz, $CDCl_3$, ppm) δ 153.7 (^1J = 237 Hz), 141.7, 137.6, 137.0, 130.1, 128.0, 127.0, 126.9, 123.1 (^3J = 8 Hz), 122.4 (^3J = 4 Hz), 120.5, 120.3, 113.7, 110.2, 106.8 (^2J = 25 Hz), 105.9 (^2J = 27 Hz).

2-bromo-9-phenyl-9H-3,9'-bicarbazole (14a) : To a solution of

carbazole (3.21 g, 19.2 mmol) in DMA (20 mL) was added 60% NaH (0.77 g, 19.2 mmol) at r.t.. After stirring for 30 min, a solution of carbazole **9** (2.18 g, 6.41 mmol) in DMA (10mL) was added. The reaction mixture was stirred at 160^{o}C for 1 day. The resulting mixture was cooled and extracted with ethyl acetate. The organic layers were dried over anhydrous $MgSO_4$ and concentrated in *vacuo*. The resulting residue was purified by using flash column chromatography on silica-gel (EA:Hex=1:10) to afford carbazole **14a** (1.11 g, 36%).

^{1}H-NMR (400 MHz, $CDCl_3$, ppm) δ 8.25 (s, 1H), 8.22 (d, *J* = 7.6 Hz, 2H), 8.05 (d, *J* = 8.0 Hz, 1H), 7.87 (s, 1H), 7.64-7.71 (m, 4H), 7.57 (t, *J* = 7.2 Hz, 1H), 7.41-7.48 (m, 4H), 7.33 (t, *J* = 7.6 Hz, 3H), 7.14 (d, *J* = 8.0 Hz, 2H). ^{13}C-NMR (100 MHz, $CDCl_3$, ppm) δ 141.8, 141.8, 141.3, 136.8, 130.2, 128.3, 128.3, 127.2, 127.2, 125.9, 123.7, 123.1, 122.6, 122.4, 121.1, 120.9, 120.6, 120.4, 119.8, 114.6, 110.4, 110.1.

2-bromo-3',6'-di-tert-butyl-9-phenyl-9H-3,9'-bicarbazole (14b) : The following the same procedure as that used for the synthesis of **14a**, the reaction of di-tert-butyl carbazole (5.01 g, 17.9 mmol), 60% NaH (0.72 g, 17.9 mmol) and carbazole **9** (3.01 g, 9.11 mmol) in DMA gave the carbazole **14b** (1.90 g, 22%) after purification by flash colmn chromatography on silica-gel (only Hex).

^{1}H-NMR (400 MHz, $CDCl_3$, ppm) δ 8.34 (s, 2H), 8.27 (s, 1H), 8.06 (d, *J* = 7.6 Hz, 1H), 7.95 (s, 1H), 7.71 (bs, 4H), 7.58-7.61 (m, 1H), 7.50-7.55 (m, 4H), 7.35 (t, *J* = 6.4 Hz, 1H), 7.13 (d, *J* = 8.4 Hz, 2H), 1.59 (s, 18H). ^{13}C-NMR (100 MHz, $CDCl_3$, ppm) δ 142.6, 141.8, 141.2, 140.5, 137.0, 130.3, 129.0, 128.3, 127.2, 127.2, 123.8, 123.7, 123.1, 122.6, 122.5, 121.3, 120.9, 120.6, 116.4, 114.5, 110.3, 109.6, 34.9, 32.2.

(9-phenyl-9H-[3,9'-bicarbazol]-2-yl)boronic acid (15a) : To a

solution of carbazole **14a** (1.03 g, 2.11 mmol) in anhydrous THF (10 mL) was slowly added 2.5 M solution of n-BuLi (1.86 mL, 4.65 mmol) at -78^{o}C. After stirring for 1 hour, a solution of trimethyl borate (0.71 mL, 6.34 mmol) in anhydrous THF (1 mL) was added at same temperature. The reaction mixture was stirred for 1 hour and for 1 hour at room temperature. A solution of HCL (1 M in water, 5 mL) was added and the biphasic mixture was vigorously stirred for another hour and then extracted with ethyl acetate. The organic layers were dried over anhydrous $MgSO_4$ and concentrated in *vacuo*. The resulting residue was purified by using short column chromatography on silica-gel (EA:Hex=1:4) to afford boronic acid **15a** (457 mg, 48%), which was used for the next step without NMR analysis data.

(3',6'-di-tert-butyl-9-phenyl-9H-[3,9'-bicarbazol]-2-yl)boronic acid (15b) : The following the same procedure as that used for the synthesis of **15a**, the reaction of 2.5 M solution of n-BuLi (2.79 mL, 6.97 mmol), trimethyl borate (1.06 mL, 9.51 mmol) and carbazole **14b** (1.90 g, 3.17 mmol) in anhydrous THF gave the boronic acid **15b** (0.75 g, 42%), which was used for the next step without NMR analysis data..

5-(9-phenyl-9H-[3,9'-bicarbazol]-2-yl)isophthalonitrile (BMK-T236) : To a solution of boronic acid **15a** (457 mg, 1.01 mmol) in THF (5 ml) was added 5-bromoisophthalonitrile (418 mg, 2.02 mmol), $Pd(PPh_3)_4$ (116 mg, 10 mol%) and a solution of K_2CO_3 (1 M in water, 2 mL) at room temperature. The reaction mixture was stirred at 80^{o}C for 12 hours. The resulting mixture was cooled and extracted with ethyl acetate. The organic layers were dried over anhydrous $MgSO_4$ and

concentrated in *vacuo*. The resulting residue was purified by using flash column chromatography on silica-gel (EA:Hex=1:10) to afford **BMK-T236** (243 mg, 45%)

^{1}H-NMR (400 MHz, $CDCl_3$, ppm) δ 8.35 (s, 1H), 8.13 (d, *J* = 8.0 Hz, 1H), 8.10 (d, *J* = 7.6 Hz, 2H), 7.65-7.73 (m, 4 H), 7.56-7.60 (m, 1H), 7.49-7.54 (m, 3H), 7.44-7.46 (m, 3H), 7.31-7.39 (m, 3H), 7.24 (t, *J* = 7.2 Hz, 2H), 7.05 (d, *J* = 8.4 Hz, 2H). ^{13}C-NMR (100 MHz, $CDCl_3$, ppm) δ 142.2, 142.2, 141.8, 140.7, 136.8, 135.5, 134.4, 133.4, 130.4, 128.4, 127.6, 127.2, 127.0, 126.2, 125.1, 123.0, 122.4, 122.2, 121.0, 121.0, 120.6, 120.2, 116.2, 113.4, 111.3, 110.4, 109.3.

5-(3',6'-di-tert-butyl-9-phenyl-9H-[3,9'-bicarbazol]-2-yl)isophthalonitrile (BMK-T237) : The following the same procedure as that used for the synthesis of **BTM236**, the reaction of boronic acid **15b** (750 mg, 1.33 mmol), 5-bromoisophthalonitrile (550 mg, 2.66 mmol), $Pd(PPh_3)_4$ (154 mg, 10 mol%) and a solution of K_2CO_3 (1 M in water, 2.7 mL) in THF gave the **BMK-T237** (590 mg, 69%).

^{1}H-NMR (400 MHz, $CDCl_3$, ppm) δ 8.28 (s, 1H), 8.08-8.10 (m, 3H), 7.65-7.72 (m, 4H), 7.55-7.59 (m, 1H), 7.46-7.54 (m, 6H), 7.32-7.38 (m, 3H), 6.94 (d, *J* = 8.8 Hz, 2H), 1.44 (s, 18H). ^{13}C-NMR (100 MHz, $CDCl_3$, ppm) δ 143.0, 142.3, 140.5, 140.5, 136.9, 135.7, 134.6, 133.8, 133.3, 130.4, 128.3, 127.8, 127.4, 127.2, 125.1, 123.9, 123.8, 123.1, 122.2, 121.0, 116.5, 116.3, 113.2, 111.3, 110.3, 108.9, 34.7, 31.9.

9-(3-Bromodibenzo[*b,d*]furan-2-yl)-9*H*-carbazole (17) : To a solution of carbazole (3.34 g, 20.0 mmol) in DMA (20 mL) was added 60% NaH (0.80 g, 20.0 mmol) at r.t.. After stirring for 30 min, a solution of dibenzofuran **16** (2.65 g, 10.0 mmol) in DMA (10mL) was

added. The reaction mixture was stirred at 160°C for 1 day. The resulting mixture was cooled and extracted with ethyl acetate. The organic layers were dried over anhydrous $MgSO_4$ and concentrated in *vacuo*. The resulting residue was purified by using flash column chromatography on silica-gel (EA:Hex=1:10) to afford carbazole **17** (1.81 g, 44%), which was used for the next step without NMR analysis data.

(2-(9H-Carbazol-9-yl)dibenzo[*b,d*]furan-3-yl)boronic acid (18) : To a solution of dibenzofuran **17** (3.70 g, 8.97 mmol) in anhydrous THF (40 mL) was slowly added 2.5 M solution of n-BuLi (7.90 mL, 19.74 mmol) at -78°C. After stirring for 1 hour, a solution of trimethyl borate (3.00 mL, 26.92 mmol) in anhydrous THF (4 mL) was added at same temperature. The reaction mixture was stirred for 1 hour and for 1 hour at room temperature. A solution of HCL (1 M in water, 20 mL) was added and the biphasic mixture was vigorously stirred for another hour and then extracted with ethyl acetate. The organic layers were dried over anhydrous $MgSO_4$ and concentrated in *vacuo*. The resulting residue was purified by using short column chromatography on silica-gel (EA:Hex=1:4) to afford boronic acid **18** (1.74 g, 51%), which was used for the next step without NMR analysis data.

9-(3-(4,6-Diphenyl-1,3,5-triazin-2-yl)dibenzo[*b,d*]furan-2-yl)-9*H*-carbazole (BMK-T317) : To a solution of boronic acid **18** (817 mg, 2.17 mmol) in THF (10 ml) was added a triazine **4** (870 mg, 3.25 mmol), $Pd(PPh_3)_4$ (250 mg, 10 mol%) and a solution of K_2CO_3 (1 M in water, 3.2 mL) at room temperature. The reaction mixture was stirred at 80°C for 12 hours. The resulting mixture was cooled and extracted with ethyl acetate. The organic layers were dried over anhydrous $MgSO_4$ and

concentrated in *vacuo*. The resulting residue was purified by using flash column chromatography on silica-gel (EA:Hex=1:10) to afford **BMK-T317** (550 mg, 45%)

^{1}H-NMR (400 MHz, $CDCl_3$, ppm) δ 8.78 (s, 1H), 8.22 (s, 1H), 8.05 (d, *J* = 7.2 Hz, 2H), 7.98-8.01 (m, 5H), 7.72 (d, *J* = 8.4 Hz, 1H), 7.59 (t, *J* = 7.6 Hz, 1H), 7.40-7.48 (m, 3H), 7.29-7.34 (m, 6H), 7.20-7.24 (m, 4H). ^{13}C-NMR (100 MHz, $CDCl_3$, ppm) δ 171.9, 171.3, 157.8, 155.6, 142.3, 135.4, 135.1, 132.3, 131.8, 128.9, 128.8, 128.3, 128.0, 126.0,123.5, 123.4, 123.3, 123.0, 121.5, 120.3, 119.4, 115.8, 112.2, 109.6.

9-(1-Bromodibenzo[*b,d*]furan-2-yl)-9*H*-carbazole (20) : The following the same procedure as that used for the synthesis of **17**, the reaction of carbazole (3.34 g, 20.0 mmol), 60% NaH (0.80 g, 20.0 mmol) and dibenzofuran **19** (2.65 g, 10.0 mmol) in DMA gave the dibenzofuran **20** (0.79 g, 19%) after purification by flash colmn chromatography on silica-gel (EA:Hex=1:10), which was used for the next step without NMR analysis data.

(2-(9*H*-carbazol-9-yl)dibenzo[*b,d*]furan-1-yl)boronic acid (21) : The following the same procedure as that used for the synthesis of **18**, the reaction of 2.5 M solution of n-BuLi (5.34 mL, 13.34 mmol), trimethyl borate (2.03 mL, 18.19 mmol) and dibenzofuran **20** (2.50 g, 6.06 mmol) in anhydrous THF gave the boronic acid **21** (1.25 g, 55%), which was used for the next step without NMR analysis data.

9-(1-(4,6-diphenyl-1s7,3,5-triazin-2-yl)dibenzo[*b,d*]furan-2-yl)-9*H*-carbazole (BMK-T318) : The following the same procedure as that used for the synthesis of **BTM317**, the reaction of boronic acid (1.25 g, 3.31 mmol), triazine **4** (1.06 g, 3.98 mmol), $Pd(PPh_3)_4$ (382 mg, 10

mol%) and a solution of K_2CO_3 (1 M in water, 4.0 mL) in THF gave the **BTM318** (990 mg, 53%).

^{1}H-NMR (500 MHz, CD_2Cl_2, ppm) δ 8.02-0.03 (m, 5H), 7.92 (d, *J* = 6.2 Hz, 2H), 7.80 (d, *J* = 6.8 Hz, 1H), 7.78 (d, *J* = 6.3 Hz, 1H), 7.72 (d, *J* = 6.7 Hz, 1H), 7.49-7.55 (m, 3H), 7.30-7.36 (m, 6H), 7.25 (d, *J* = 6.5 Hz, 2H), 7.13-7.19 (m, 3H). ^{13}C-NMR (100 MHz, $CDCl_3$, ppm) δ 171.7, 171.4, 157.4, 156.1, 142.3, 135.2, 132.5, 132.2, 131.6, 128.9, 128.5, 128.4, 128.3, 125.8, 124.4, 123.8, 123.1, 123.0, 122.9, 120.2, 119.5, 114.5, 111.9, 109.9.

Reference

1. Schmidt, J.G. *Ber. Dtsch. Chem. Ges.,* **1880**, *13*, 2342

2. Schmidt, J.G. *Ber. Dtsch. Chem. Ges.,* **1881**, *14*, 1459.

3. L. Claisen and A. Claparède, *Ber. Dtsch. Chem. Ges.,* **1881**, *14*, 349.

4. W. S. Rapson and R. Robinson *J. Chem. Soc.,* **1935**, 1285

5. G. Wittig and G. Geissler, *Liebigs Ann*., **1953**, *580*, 44.

6. G. Stork and A. G. Schultz, *J. Am. Chem. Soc.,* **1971**, *93*, 4074.

7. E. J. Corey and H. E. Ensley, *J. Am. Chem. Soc.,* **1975**, *97*, 6908.

8. D. A. Evans, E. Vogel and J. V. Nelson, *J. Am. Chem. Soc*.**, 1979**, *101*, 6120

9. D. A. Evans, J. Bartroli and T. L. Shih, *J. Am. Chem. Soc*.**, 1981**, *103*, 2127.

10. D. A. Evans, *Aldrichimica Acta***, 1982**, *15*, 23.

11. B. E. Maryanoff and A. B.Reitz, *Chem*. *Rev*., **1989**, *89*, 863.

12. R. F. Heck, *J. Am. Chem. Soc*.**, 1968**, *90*, 5518.

13. T. Mizoroki, K. Mori and A. Ozaki, *Bull. Chem. Soc. Jpn.*, **1971**, *44*, 581.

14. R. F. Heck, J. P. Nolley, Jr., *J. Org. Chem.* **1972**, *37*, 2320

15. M. Kosugi, K. Sasazawa, Y. Shimizu and T. Migita, *Chem. Lett.,* **1977**, 301.

16. M. Kosugi, Y. Shimizu and T. Migita, *Chem. Lett.,* **1977**, 1423.

17. Y. Hatanaka and T. Hiyama, *J. Org. Chem.,* **1988**, *53*, 918.

18. N. Miyaura, K. Yamada and A. Suzuki, *Tetrahedron Lett.,* **1979**, 3437.

19. N. Miyaura and A. Suzuki, *Chem. Comm.,* **1979**, 866.

20. N. Miyaura and A. Suzuki, *Chem. Rev.,* **1995**, *95*, 2457.

21. L. Yin and J. Liebscher, *Chem. Rev*., **2007**, *107*, 133.

22. N. Miyaura and A. Suzuki, *Chem. Rev*., **1955**, *95*, 2457.

23. L. Xue and Z. Lin, *Chem. Soc. Rev.,* **2010**, *39*, 1692.

24. Q. xiao, S. Sarina, E. jaatinen, J. Jia, D. P. Arnold and H.Zhu, *Green chem.,* **2014**, *16*, 4272.

25. A. Fihri, M. Bouhrara, B. Nekoueishahraki, J. M. Basset and V. Polshettiwar, *Chem. Soc. Rev.,* **2011**, *40*, 5181.

26. B. J. Borah, K. Saikia, P. P. Saikia, N. C. Barua and D. K. Dutta, *Catal. Today,* **2012**, *198*, 174.

27. R. K. Rai, K. Gupta, S. Behrens, J. Li, Q. Xu and S. K. Singh, *ChemCatChem,* **2015**, *7*, 1806.

28. B. Yuan, Y. Pan, Y. Li, B.Yin and H. Jiang, *Angew. Chem. Int. Ed.,* **2010**, *49*, 4054.

29. Z. J. Wang, S. Ghasimi, K. Landfester and K. A. I. Zhang, *Chem. Mater.,* **2015**, *27*, 1921.

30. K. Y. Cho, H. Y. Seo, Y. S. Yeom, P. Kumar, A. S. Lee, K. –Y. Baek and H. G. Yoon, *Carbon,* **2016**, *105*, 340.

31. Y. Jang, J. Chung, S. Kim, S. W. Jun, B. H. Kim, D. W. Lee, B. M. Kim and T. Hyeon, *Phys. Chem. Chem. Phys.,* **2011**, *13*, 2512.

32. I. Nakamura and Y. Yamamoto, *Chem. Rev.*, **2004**, *104*, 2127.

33. B. M. Trost, Wiley-VCH: Weinheim, **2004**, pp 2-14.

34. L. Anastasia and E. Negishi, Wiley: New York, **2002**, pp 311-344.

35. D. S. Surry and S. L. Buchwald, *Chem. Sci.*, **2011**, *2*, 27.

36. E. A. Kantchev and C. J. O'Brien, *Angew. Chem. Int. Ed.*, **2007**, *46*, 2768.

37. G. Dhangar, J. L. Serrano, C. Schulzke, K. C. Gunturu and A. R. Kapdi, *ACS Omega*, **2017**, *2*, 3144.

38. M. A. Baldo, M. E. Thompson and S. R. Forrest, *Nature*, **2000**, *403*, 750.

39. J. J. Halls, C. A. Walsh, N. C. Greenham, E. A. Marseglia, R. H. Friend, S. C. Moratti and A. B. Holmes, *Nature*, **1995**, *376*, 498.

40. J. N. Moorthy, P. Venkatakrishnan, P. Natarajan, D. F. Huang and T. J. Chow, *J. Am. Che. Soc.*, **2008**, *130*, 17320.

41. L. Wang, W. Y. Wong, M. F. Lin, W. K. Wong, K. W. Cheah, H. L. Tam and C.H. Chen, *J. Mater. Chem.*, **2008**, *18*, 4529.

42. M. S. Gong, H. S. Lee and Y. M. Jeon, *J. Mater. Chem.*, **2010**, *20*, 10735.

43. J. Kido, M. Kimura and K. Nagai, *Science,* **1995**, *267*, 1332.

44. Y. Sun, N. C. Giebink, H. Kanno, B. Ma, M. E. Thompson and S. R. Forrest, *Nature,* **2006**, *440*, 908.

45. S. Reineke, F. Lindner, G. Schwartz, N. Seidler, K. Walzer, B. Lussem and K. Leo *Nature,* **2009**, *459*, 234.

46. T-. H. Han, Y. Lee, M-. R. Choi, S-. H. Woo, S-.H. Bae, B. H. Hong, J-. H. Ahn and T-. W. Lee, *Nat. Photonics,* **2012**, *6*, 105.

47. T. Chen, Lei. Zheng, J. Yuan, Z. An, R. Chen, Y. Tao, H. Li, X. Xie and W. Huang *Sci. Rep.*, **2015**, *5*, 10923.

48. R. Komatsu, T. Ohsawa, H. Sasabe, K. Nakao, Y. Hayasaka and J. Kido, *ACS Appl. Mater. Inter.,* **2017**, *9*, 4742.

49. K. Sato, K. Shizu, K. Yoshimura, A. Kawada, H. Miyazaki and C. Adachi, *Phys. Rev. Lett.*, **2013**, *110*, 247401.

50. D. Voz, *J. Photonics Energy,* **2016**, *6*, 02091.

51. Z. Yang, Z. Mao, Z. Xie, Y. Zhang, S. Liu, J. Zhao, J. Xu, Z. Chi and M. P. Aldred, *Chem. Soc. Rev.*, **2017**, *46*, 915.

52. G. M. Scheuermann, L. Rumi, P. Steurer, W. Bannwarth and R. Mülhaupt, *J. Am. Chem. Soc.,* **2009**, *131*, 8262.

53. H. Q. Song, Q. Zhu, X. J. Zheng and X. G. Chen, *J. Mater. Chem. A,* **2015**, *3*, 10368.

54. A. Ohtaka, J. M. Sansano, C. Nájera, I. Miguel-García, Á. Berenguer-Murcia and D. Cazorla-Amorós, *ChemCatChem,* **2015**, *7*, 1841.

55. S. I. Yamamoto, H.Kinoshita, H. Hashimoto and Y. Nishina, *Nanoscale,* **2014**, *6*, 6501.

56. Y. Yang, D. Cong and S. Hao, *ChemCatChem,* **2016**, *8*, 900.

57. J. Sun, Y. Fu, G. He, X. Sun and X. Wang, *Appl. Catal. B,* **2015**, *165*, 661.

58. M. Hajighorbani and M. Hekmati, *RSC Adv.,* **2016**, *6*, 88916.

59. Y. Li, X. Fan, J. Qi, J. Ji, S. Wang, G. Zhang and F. Zhang, *Nano Res.,* **2010**, *3*, 429.

60. A. R. Siamaki, A. E. R. S. Khder, V. Abdelsayed, M. S. El-Shall and B. F. Gupton, *J. Catal.*, **2011**, *279*, 1.

61. Z. Zhang, T. Sun, C. Chen, F. Xiao, Z. Gong and S. Wang, *ACS Appl. Mater. Interfaces,* **2014**, *6*, 21035.

62. X. Gu, W. Qi, X. Xu, Z. Sun, L. Zhang, W. Liu, X. Pan and D. Su, *Nanoscale,* **2014**, *6*, 6609.

63. S. Bai and X. Shen, *RSC Adv.,* **2012**, *2*, 64.

64. V. Georgakilas, M. Otyepka, A. B. Bourlinos, V. Chandra, N. Kim, K. C. Kemp, P. Hobza, R. Zboril and K. S. Kim, *Chem. Rev.*, **2012**, *112*, 6156.

65. K. Y. Cho, Y. –J. Lee, H. –J. Kim, H. G. Yoon, S. S. Hwang, Y. –K. Han and K. –Y. Baek, *Polymer*, **2015**, *77*, 55.

66. G. Fu, L. Tao, M. Zhang, Y. Chen, Y. Tang, J. Lin and T. Lu, *Nanoscle*, **2013**, *5*, 8007.

67. K. Y. Cho, Y. S. Yeom, H. Y. Seo, Y. H. Park, H. N. Jang, K. –Y. Baek and H. G. Yoon, *ACS Appl. Mater. Interfaces,* **2015**, *7*, 9841.

68. D. S. Su, S. Perathoner and G. Centi, *Chem. Rev.,* **2013**, *113*, 5782.

69. K. Y. Cho, Y. S. Yeom, H. Y. Seo, P. Kumar, A. S. Lee, K. –Y. Baek and H. G. Yoon, *J. Mater. Chem. A,* **2015**, *3*, 20471.

70. K. Y. Cho, Y. S. Yeom, H. Y. Seo, P. Kumar, A. S. Lee, K. –Y. Baek and H. G. Yoon, *ACS Appl. Mater. Interfaces,* **2017**, *9*, 1524.

71. R. Narayanan and M. A. El-sayed, *J. Phys. Chem. B,* **2004**, *108*, 8572.

72. K. Y. Cho, Y. S. Yeom, H. Y. Seo, P. Kumar, K. –Y. Baek and H. G. Yoon, *J. Mater. Chem. A,* **2017**, *5*, 3129.

73. M. Zhu and G. Diao, *J. Phys. Chem. C,* **2011**, *115*, 24743.

74. S. P. Andrews, A. F. Stepan, H. Tanaka, S. V. Ley and M. D. Smith, *Adv. Synth. Catal.,* **2005**, *347*, 647.

75. A. Zhang, M. Liu, M. Liu, Y. Xiao, Z. Li, J. Chen, Y. Sun, J. Zhao, S. Fang, D. Jia and F. Li, *J. Mater. Chem. A,* **2014**, *2*, 1369.

76. P. Zhang, Z. Weng, J. Guo and C. Wang, *Chem. Mater.*, **2011**, *23*, 5243.

77. E. Kim, H. S. Jeong and B. M. Kim, *Catal. Commun.,* **2014**, *46*, 71.

78. H. Yuan, H. Liu, B. Zhang, L. Zhang, H. Wang and D. S. Su, *Phys. Chem. Chem. Phys*., **2014**, *16*, 11178.

79. S. Byun, J. Chung, J. Kwon and B. M. Kim*, Chem. Asian J.,* **2015**, *10*, 982.

80. H. Uoyama, K. Goushi, K. Shizu, H. Nomura and C. Adachi, *Nature*, **2012**, *492*, 234.

81. Y. Tao, K. Yuan, T. Chen, P. Xu, H. Li, R. Chen, C. Zheng, L. Zhang and W. Huang, *Adv. Mater*. **2014**, *26*, 7931.

82. Q. Zhang, B. Li, S. Huang, H. Nomura, H. Tanaka and C. Adachi, *Nat. Photonics*, **2014**, *8*, 326.

83. S. Hirata, Y. Sakai, K. Masui, H. Tanaka, S. Y. Lee, H. Nomura, N. Nakamura, M. Yasumatsu, H. Nakanotani, Q. Zhang, K. Shizu, H. Miyazaki and C. Adachi, *Nat. Mater.*, **2015**, *14*, 330.

84. Q. Zhang, D. Tsang, H. Kuwabara, Y. Hatae, B. Li, T. Takahashi, S. Y. Lee, T. Yasuda and C. Adachi, *Adv. Mater.*, **2015**, *27*, 2096

85. M. Kim, S. K. Jeon, S-.H. H and J. Y. Lee, *Adv. Mater.*, **2015**, *27*, 2515.

86. J. W. Sun, J. Y. Baek, K-. H. Kim, C-. K. Moon, J-. H. Lee, S-. K. Kwon, Y-. H. Kim and J-. J. Kim, *Chem. Mater.*, **2015**, *27*, 6675.

87. S. Y. Lee, T. Yasuda, H. Nomura and C. Adachi, *Appl. Phys. Lett.*, **2012**,

101, 093306.

88. P. Rajamalli, N. Senthilkumar, P. Gandeepan, C-.C. Ren-Wu, H-. W. Lin and C-. H. Cheng, *ACS Appl. Mater. Interfaces*, **2016**, *8*, 27026.

89. Y. Yang, S. Wang, Y. Zhu, Y. Wang, H. Zhan and Y. Cheng, *Adv. Funct. Mater.*, **2018**, *28*, 1706916.

90. Y-. S. Park, S. Lee, K-. H. Kim, S-. Y. Kim, J-. H. Lee and J-. J. Kim, *Adv. Funct. Mater.*, **2013**, *23*, 4914.

91. Y. J. Cho, B. D. Chin, S. K. Jeon and J. Y. Lee, *Adv. Funct. Mater.,* **2015**, *25*, 6786.

92. W. Liu, C-. J. Zheng, K. Wang, Z. Chen, D-. Y. Chen, F. Li, X-. M. O, Y-. P. Dong and X-. H. Zhang, *ACS Appl. Mater. Interfaces*, **2015**, *7*, 18930.

93. Y. J. Cho, S. K. Jeon, S-. S. Lee, E. Yu and J. Y. Lee, *Chem. Mater.*, **2016**, *28*, 5400.

94. J. S. Kang, T. R. Hong, H. J. Kim, Y. H. Son, R. Lampande, B. Y. Kang, C. Lee, J-. K. Bin, B. S. Lee, J. H. Yang, J. Kim, S. Park, M. J. Cho, J. H. Kwon and D. H. Choi, *J. Mater. Chem. C*, **2016**, *4*, 4512.

95. Y. H. Lee, H. Park, J. Oh, J. W. Shin, J. Jung, S. Yoo and M. H. Lee, *ACS Appl. Mater. Interfaces*, **2017**, *9*, 24035.

96. P. Rajamalli, V. Thangaraji, N. Senthilkumar, C-. C. Ren-Wu, H-. Wu. Lin and C-. H. Cheng, *J. Mater. Chem. C*, **2017**, *5*, 2919.

97. D. Zhang, X. Song, M. Cai, H. Kaji and L. Duan, *Adv, Mater*, **2018**, *30*, 1705406.

98. X-. K. Chen, Y. Tsuchiya, Y. Ishikawa, C. Zhong, C. Adachi and J-. L. Bredas, *Adv. Mater.*, **2017**, *29*, 1702767.

99. H. Fukagawa, T. Shimizu, Y. Iwasaki and T. Yamamoto, *Sci. Rep.*, **2017**, *7*, 1735.

100. W. Zhang, Y.-X. Zhang, X.-Q. Zhang, X.-Y. Liu, J. Fan and L.-S. Liao, *Org. Electron.*, **2018**, *58*, 238.

101. J. Li, X. Liao, H. Xu, L. Li, J. Zhang, H. Wang and B. Xu, *Dyes Pigm.*, **2017**, *140*. 79.

102. P. Rajamalli, N. Senthilkumar, P.-Y. Huang, C.-C. Ren-Wu, H.-W. Lin and C.-H. Cheng, *J. Am. Chem. Soc.,* **2017**, *139*. 10948.

103. S.-J. Woo, Y. Kim, S.-K. Kwon, Y.-H. Kim and J.-J. Kim, *ACS Appl. Mater. Interfaces,* **2019**, *11*, 7199.

104. Y. Wada, S. Kubo, H. Kaji, *Adv. Mater.*, **2018**, *30*, 1705641.

105. R. Komatsu, T. Ohsawa, H. Sasabe, K. Nakao, Y. Hayasaka and J. Kido, *ACS Appl. Mater. Interfaces*, **2017**, *9*, 4742.

106. Y. Im, S. H. Han and J. Y. Lee, *J. Mater. Chem. C*, **2018**, *6*, 5012.

107. C.-Y. Chan, L.-S. Cui, J. U. Kim, H. Nakanotani and C. Adachi, *Adv. Funct. Mater.*, **2018**, *28*, 1706023.

108. X. Liang, H.-B. Han, Z.-P. Yan, L. Liu, Y.-X. Zheng, H. Meng and W. Huang, *New J. Chem.*, **2018**, *42*, 4317.

109. J. S. Ward, R. S. Nobuyasu, A. S. Batsanov, P. Data, A. P. Monkman, F. B. Dias and M. R. Bryce, *Chem. Commun.*, **2016**, *52*, 2612.

110. A. P. Antonchick, R. Samanta, K. Kulikov and Jonas Lategahn, *Angew. Chem. Int. Ed.*, **2011**, *50*, 8605.

111. C-. H. Siu, C-. L. H, J. He, T. Chen, P. Majumda, J. Zhao, H. Li and W-. Y. Wong, *Polyhedron*, **2014**, 82, 71.

112. J. C. Holder, E.D. Goodman, K. Kikushima, M. Gatti, A. N. Marziale and B. M. Stoltz, *Tetrahedron*, **2015**, 71, 5781.

113. P. J. Stephens, F.J. Devlin, C.F. Chabalowski, M. J. Frishch, *J. Phys. Chem.*, **1994**, *98*, 11623.

114. Y. Zhao, D.G. Truhlar, *J. Phys. Chem. A*, **2004**, *108*, 6908.

115. P. K. Samanta, D. Kim, V. Coropceanu, J. -L. Bredas, *J. Am. Chem. Soc*., **2017**, *139*, 4042.

116. R. A. Marcus, *J. Chem. Phys.*, **1956**, *24*, 966.

117. S. Feng, K. Wen, Y. Si, X. Guo, J. Zhang, *J. Comput. Chem.*, **2018**, *39*, 2601.

118. Gaussian 09, Revision E.01, M. J. Frisch et al., Gaussian, Inc., Wallingford CT, 2009.

119. ADF2016, SCM, Theoretical Chemistry, Vrije Universiteit, Amsterdam, The Netherlands, E.J. Baerends et al.

120. A. Endo, K. Yoshimura, T. Kai, A. Kawada, H. Miyazaki, C. Adachi, *Appl. Phys. Lett.*, **2011**, *98*, 083302.

121. G. Méhes, H. Nomura, Q. Zhang, T. Nakagawa, C. Adachi, *Angew. Chem. Int. Ed*., **2012**, *51*, 11311.

122. H. Tanaka, K. Shizu, H. Miyazaki, C. Adachi, *Chem. Commun*., **2012**, *48*, 11392.

123. Q. Zhang, J. Li, K. Shizu, S. Huang, S. Hirata, H. Miyazaki, C. Adachi, *J. Am. Chem. Soc*., **2012**, *134*, 14706.

124. Q. Zhang, H. Kuwabara, Jr. W. J. Potscavage, S. Huang, Y. Hatae, T. Shibata, C. Adachi, *J. Am. Chem. Soc*., **2014**, *136*, 18070.

125. K. Shizu, H. Tanaka, M. Uejima, T. Sato, K. Tanaka, H. Kaji, C. Adachi, *J. Phys. Chem. C,* **2015**, *119*, 1291.

126. M. W. Cooper, X. Zhang, Y. Zhang, S. O. Jeon, H. Lee, S. Kim, C. Fuentes-Hernandez, S. Barlow, B. Kippelen and S. R. Marder, *Chem. Mater.*, **2018**, *30*, 6389.

127. J. G. Yu, S. H. Han, H. L. Lee, W. P. Hong and J. Y. Lee, *J. Mater. Chem. C.*, **2019**, *7*, 2919.

128. M. W. Cooper, X. Zhang, Y. Zhang, S. O. Jeon, H. Lee, S. Kim, C. Fuentes-Hernandez, S. Barlow, B. Kippelen and S. R. Marder, *Chem. Mater.*, **2018**, *30*, 6389.

129. S. □G. Ihn, N. Lee, S. O. Jeon, M. Sim, H. Kang, Y. Jung, D. H. Huh, Y. M. Son, S. Y. Lee, M. Numata, H. Miyazaki, R. G□Bombarelli, J. A. Parraguirre, T. Hirzel, A. Aspuru–Guzik, S. Kim and S. Lee, *Adv. Sci.*, **2017**, *4*, 1600502.

국문 초록

I. 이온성 고분자로 조정된 재사용 가능한 팔라듐-그래핀 하이브리드 촉매를 사용한 효율적인 스즈키 결합 반응 연구

팔라듐 나노 촉매의 단점인 재사용 및 반응성의 어려움을 극복하기 위하여, 이온성 고분자로 조정된 팔라듐-그래핀 하이브리드 촉매를 개발하였다. 위 촉매의 반응성을 확인하기 위하여, 스즈키 결합 반응에 접목시켜 촉매의 성능을 측정하였다. 이온성 고분자의 영향이 팔라듐 나노 촉매가 그래핀위에서 고르게 분포 될 수 있도록 도와주었으며, 또한 유기물질들의 상호작용덕분에 반응성이 증가한 것을 확인 하였다. 이온성 고분자가 없는 일반 팔라듐-그래핀 촉매와 비교하였을 때, 이온성 고분자로 조정된 팔라듐-그래핀 촉매는 16배 이상의 촉매 성능을 나타냈다. 기존 논문들에서 보고된 팔라듐 나노 촉매와 비교하여 성능이 향상되었음을 확인하였고, 촉매의 재사용에 대한 연구도 진행하였다. 10번 이상의 재사용 실험을 반복 실험 하였으며, 모두 96% 이상의 높은 수득률을 보였다. 고온-여과 실험 및 반응 전/후 전자현미경을 통한 분석으로부터, 촉매의 유의한 침출현상은 발생하지 않음을 증명하였다.

Ⅱ. 탄소-탄소 결합으로 연결된 전자 주개와 받개를 특징으로 하는 새로운 열 활성 지연 청색 형광 분자 디자인에 대한 설계 전략 연구

열 활성 지연 형광 (TADF) 기술의 짧은 재료 수명은 효율적이며 내구성이 뛰어난 장치 개발에 있어서 큰 장애물로 여겨진다. 재료의 안정성을 높이기 위하여, 주개-받개 사이의 결합을 기존에 주로 사용하는 방식(탄소-질소 결합)과 다르게 탄소-탄소 결합을 가지며, 입체적으로 뒤틀린 결합구조를 가지는 분자를 고안 및 합성하였다. 대조 화합물 (CPT2)과 비교하여, 분자내의 상반각이 30배 이상 증가하고 단일항-삼중항 에너지 준위 차이가 0.22 eV 만큼 감소하였다.

핵심구조를 카바졸에서 디벤조퓨란으로 변경함으로써, BMK-T317과 BMK-T318 화합물은 높은 외부 양자 효율을 나타냈다(EQE = 19.9% 그리고 18.8%). 또한, 화합물의 안정성 검사에서도 상당한 향상을 보였다. 그러므로, 탄소-탄소 결함을 가진 TADF 방출체 화합물은 청색 형광 분자의 고효율 및 장수명에 대한 가능성을 보였다.

Spectral Data

Characterization data of products

2-Bromo-3-fluoro-9H-carbazole (8)

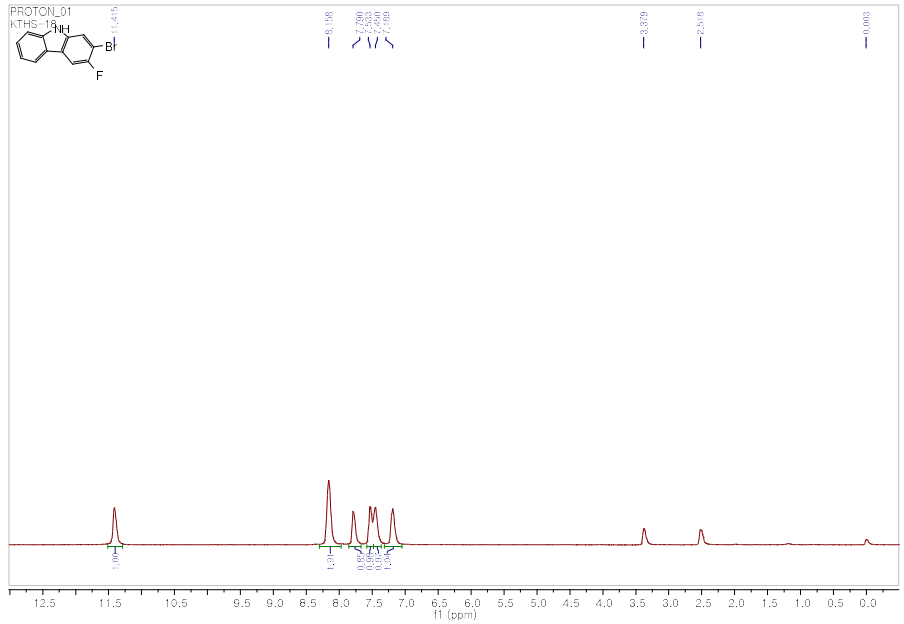

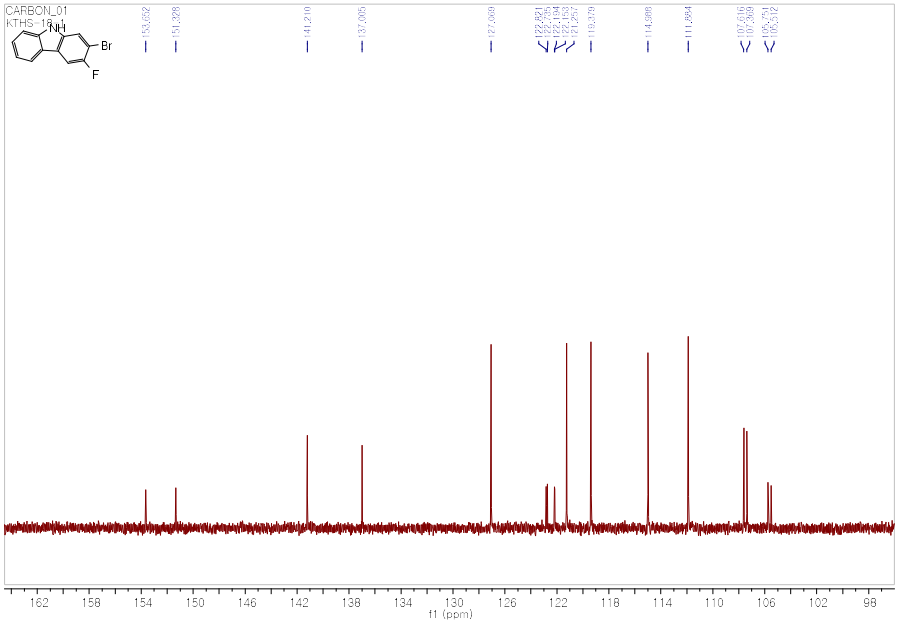

2-Bromo-3-fluoro-9-phenyl-9H-carbazole (9)

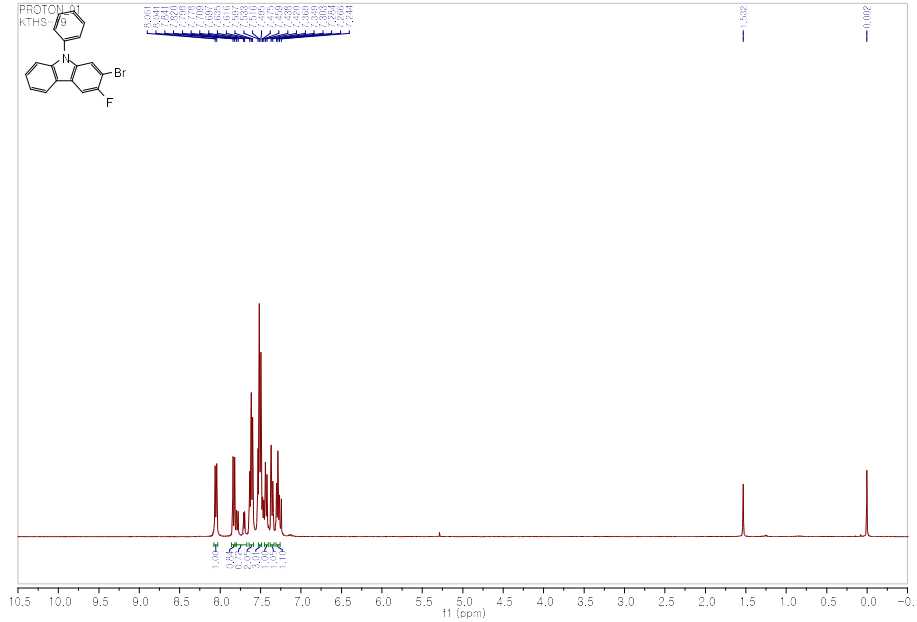

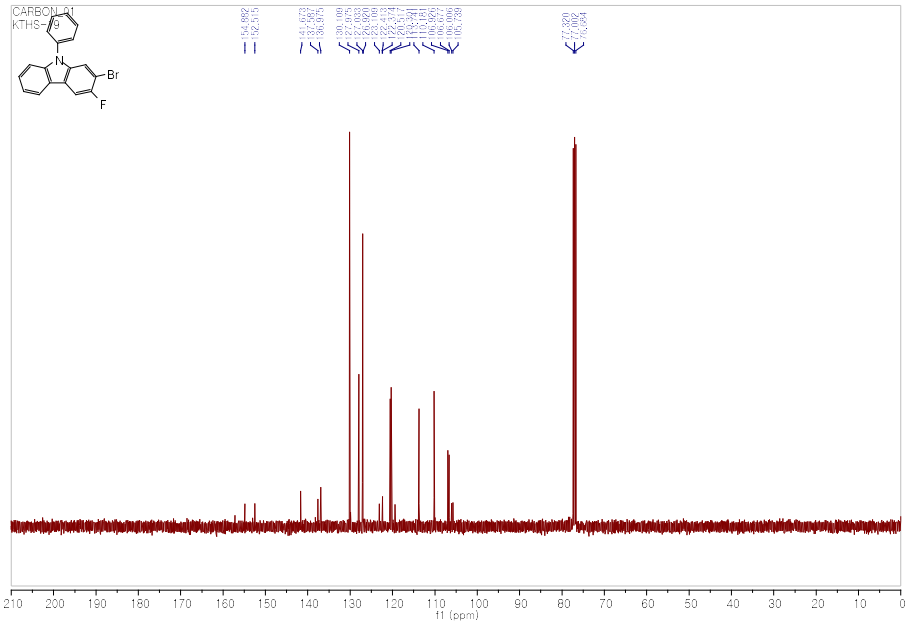

2-bromo-9-phenyl-9H-3,9'-bicarbazole (14a)

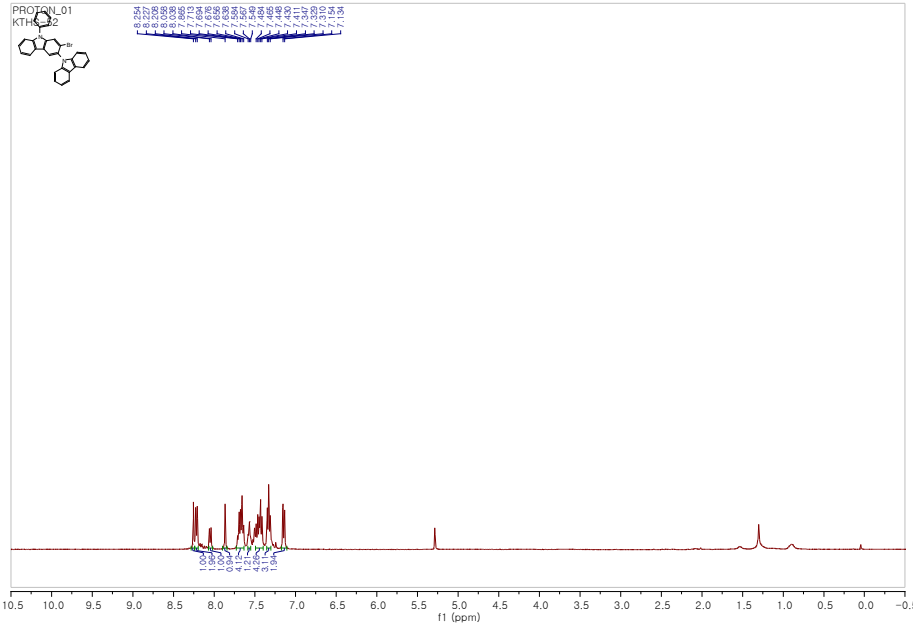

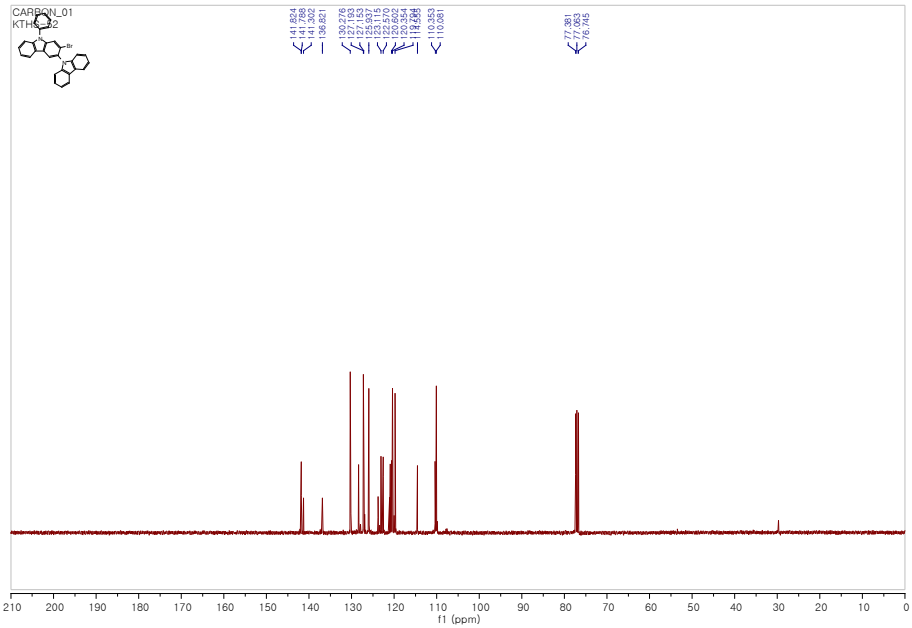

2-bromo-3',6'-di-tert-butyl-9-phenyl-9H-3,9'-bicarbazole (14b)

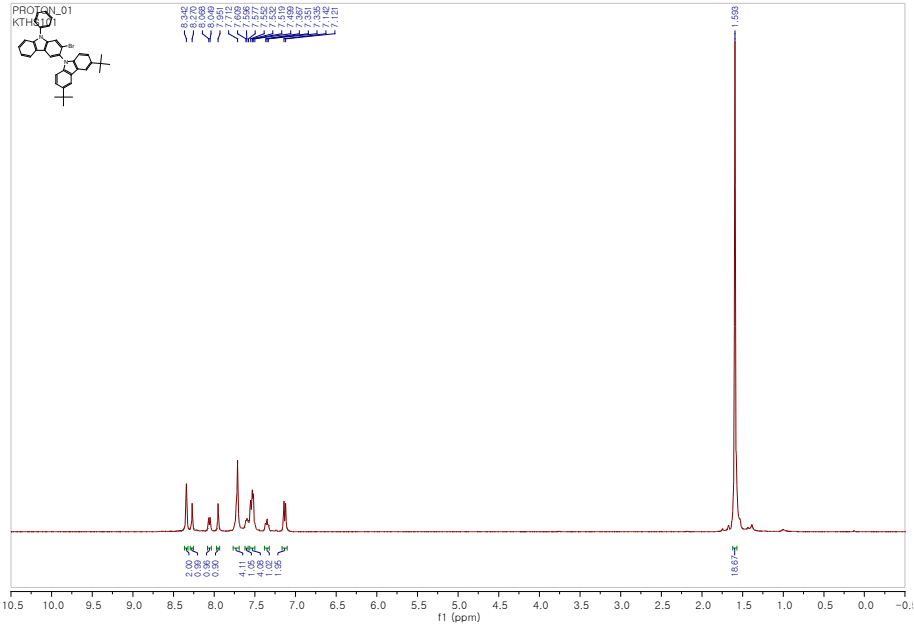

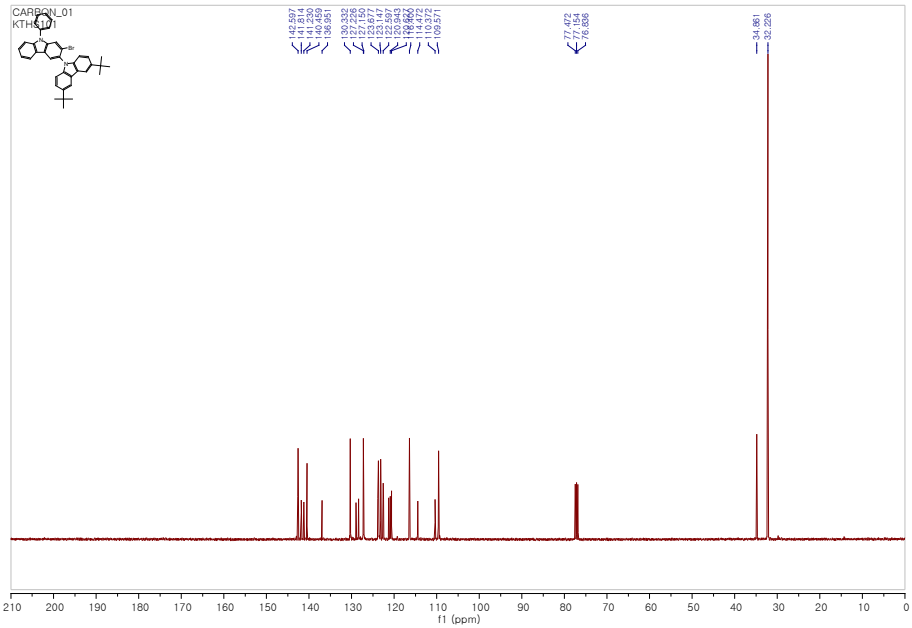

5-(9-phenyl-9H-[3,9'-bicarbazol]-2-yl)isophthalonitrile (BMK-T236)

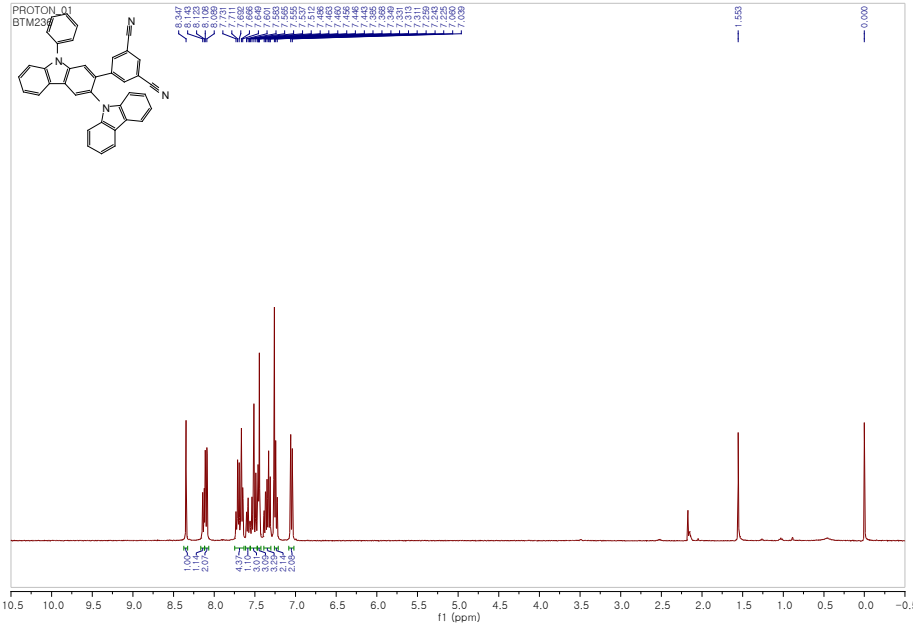

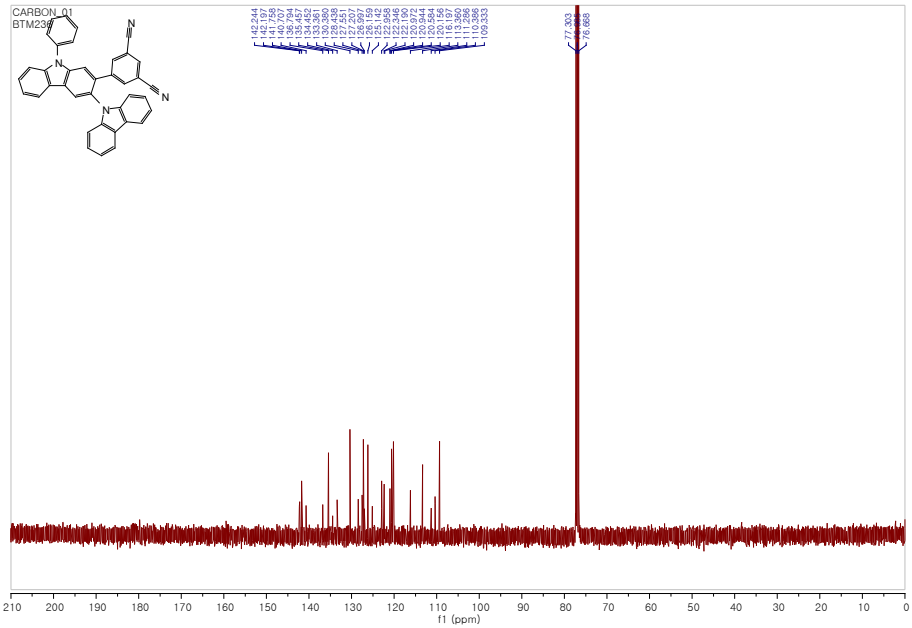

5-(3',6'-di-tert-butyl-9-phenyl-9H-[3,9'-bicarbazol]-2-yl)isophthalonitrile (BMK-T237)

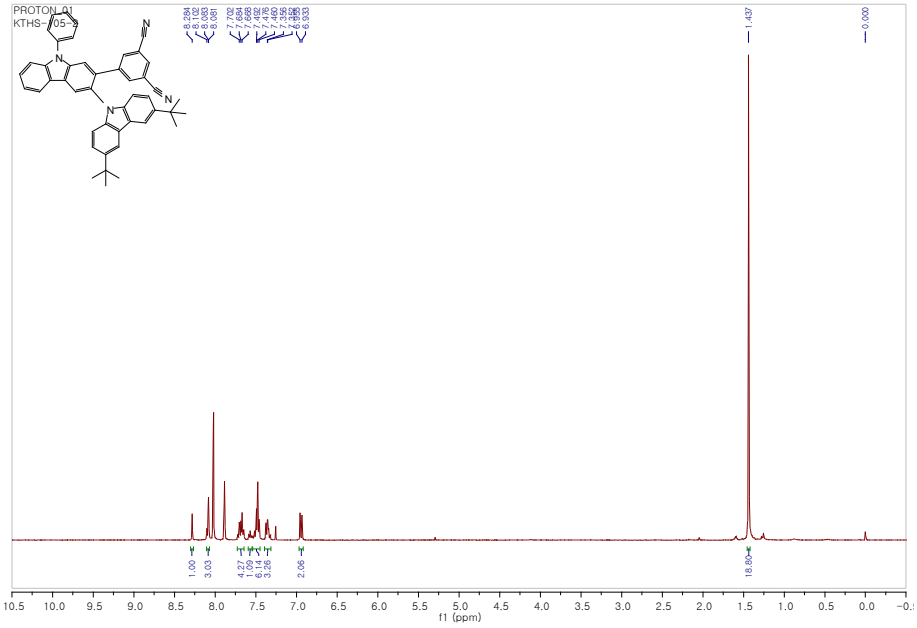

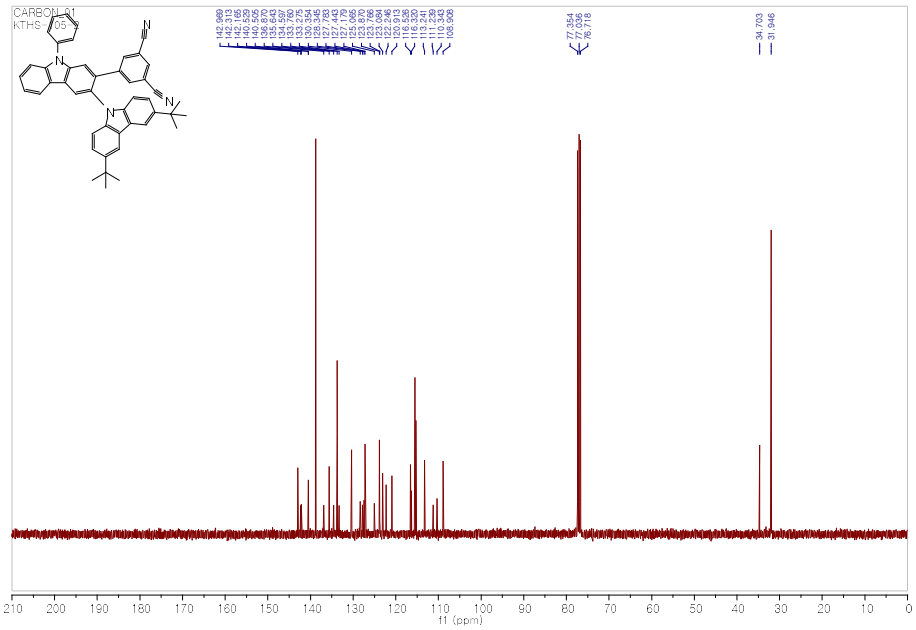

9-(3-(4,6-Diphenyl-1,3,5-triazin-2-yl)dibenzo[*b,d*]furan-2-yl)-9*H*-carbazole (BMK-T317)

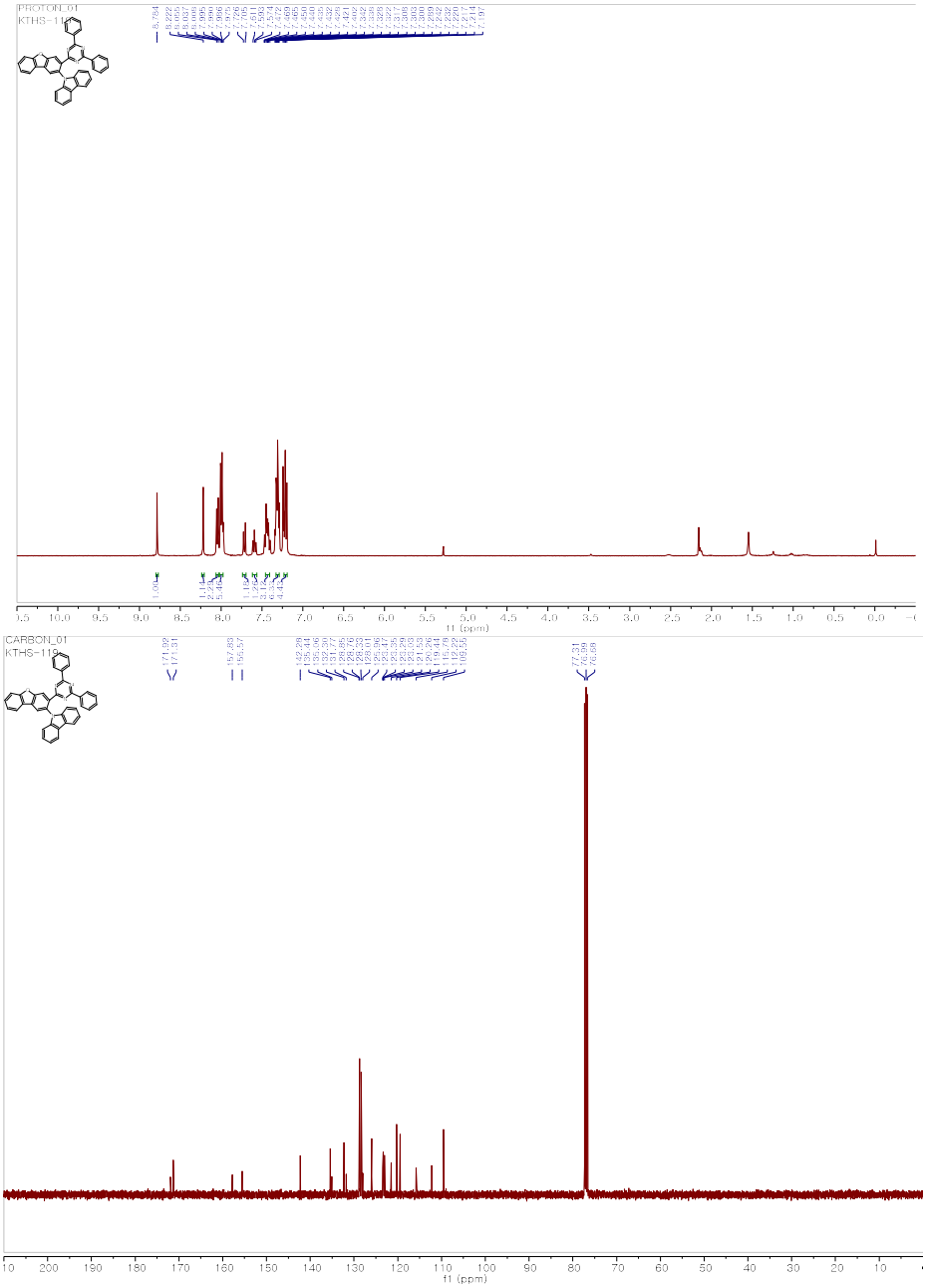

9-(1-(4,6-diphenyl-1s7,3,5-triazin-2-yl)dibenzo[*b,d*]furan-2-yl)-9*H*-carbazole (BMK-T318)